General Disclaimer

One or more of the Following Statements may affect this Document

- This document has been reproduced from the best copy furnished by the organizational source. It is being released in the interest of making available as much information as possible.

- This document may contain data, which exceeds the sheet parameters. It was furnished in this condition by the organizational source and is the best copy available.

- This document may contain tone-on-tone or color graphs, charts and/or pictures, which have been reproduced in black and white.

- This document is paginated as submitted by the original source.

- Portions of this document are not fully legible due to the historical nature of some of the material. However, it is the best reproduction available from the original submission.

AS&E

**American Science
and Engineering, Inc.**

955 Massachusetts Avenue
Cambridge, Massachusetts 02139
617-868-1600   Telex 921-458

30 JUNE 1981

ASE-4649

FINAL REPORT ON:

THE APPLICATION OF SOFT X-RAY IMAGING TECHNIQUES TO AURORAL RESEARCH

CONTRACT NASW-3426

PREPARED FOR:

PLASMA PHYSICS BRANCH

**NATIONAL AERONAUTICS
AND SPACE ADMINISTRATION**

WASHINGTON, D.C.   20546
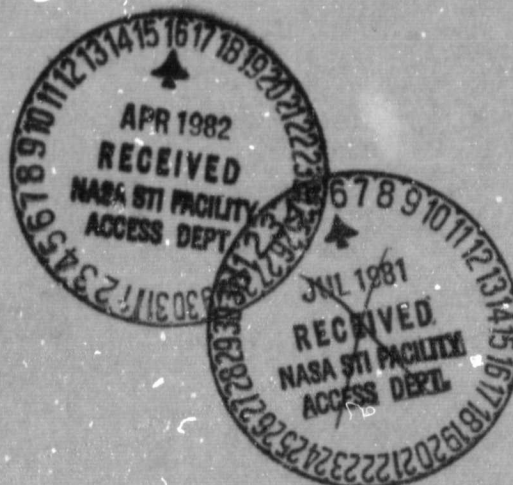
Final Report on

THE APPLICATION OF
SOFT X-RAY IMAGING TECHNIQUES
TO AURORAL RESEARCH

Contract NASW-3426

Prepared for:
Plasma Physics Branch
National Aeronautics and Space Administration
Washington, D.C.   20546

Prepared by:
American Science and Engineering, Inc.
955 Massachusetts Avenue
Cambridge, MA   02139

30 June 1981

Approved:

David M. Rust

TABLE OF CONTENTS

1.0   INTRODUCTION AND SUMMARY

The use of soft X-ray imaging telescopes is now accepted as a
powerful tool for astrophysical studies. Over the past twenty
years there have been major improvements in the ability to image
sources of soft X-ray emission using the techniques of grazing
incidence optics. X-ray telescopes flown on sounding rockets have
provided images of the sun over the past solar cycle. The solar
X-ray telescope on Skylab provided us with high-resolution, broad-
band, wide-field images of the sun which led to new insights into
the physics of the solar corona. The results of the Einstein
Observatory, which has imaged numerous astrophysical objects, are
well known.

One area which has remained unexplored by grazing incidence optics
techniques is the earth's auroral zones. Hard X-rays (E > 10 keV)
from these regions have been observed from balloon-borne and
satellite-borne experiments for a number of years. The X-ray
emission has been found to be well correlated with energetic
particle precipitation. From current theoretical work and from
downward extrapolations of higher energy observations, it is clear
that most of the X-radiation from precipitating particles will be
in the 0.3 - 3.0 keV band. With suitable instrumentation, then,
the intense, soft X-rays can be shaped into detailed pictures of
the auroral zones.

For lack of an appropriate instrument and flight opportunity the
0.3 - 3.0 keV spectral range has not been used in magnetospheric
studies before. We cannot guess what discoveries will follow the
exploration of this field, but advances in X-ray astronomy have
always produced dramatic and exciting new results.

The purpose of this report is to discuss the feasibility of
building and operating a grazing incidence X-ray telescope for

auroral zone X-ray studies from a satellite. The satellite
assumed in the study was the Polar Plasma Laboratory (PPL) of the
proposed NASA mission to investigate the Origins of Plasma in the
Earth's Neighborhood (OPEN). The PPL was selected as the optimum
satellite because of both its high inclination to the earth's
equator, which affords a good view of the polar regions, and its
optimal orbital apogee of 15 R_e and, later, 4 R_e which provide
reasonable fields of view for the telescope.

The most important result of our study is that there is no barrier
to the feasibility of studying the auroral zones with a grazing
incidence X-ray telescope. We have performed trade-offs among
several designs of X-ray telescopes to select a design which is
well matched to the requirements of auroral zone studies. The
discussion of design principles appears in Section 2. In Section
2.3, we present our detailed structural analysis of the preferred
design, an array of seven nested Wolter mirrors. We have prepared
an engineering evaluation of the requirements for the instrumental
configuration, power, weight, and telemetry. In addition, the
problems of radiation hardening and thermal control have been
studied. The resulting strawman instrument is presented and
discussed in Section 6.

A key component of the instrument is the detector, for which we
have selected a charge-coupled device (CCD). CCD's have been
widely used as optical detectors and are now being used as X-ray
and XUV detectors, for example, on the American Science and
Engineering X-ray/XUV solar telescope for the International Solar
Polar Mission. In large X-ray fluxes CCD's may be operated as
energy flux detectors, but they do not record the number or
energies of individual incident photons. With the expected low
flux intensities from auroral emissions, the possibility arises of
reading out the accumulated charge on the CCD fast enough to
detect the energies of single photons and thereby derive an energy

spectrum. A discussion of the work we have done to show the feasibility of this technique is given in Section 5.

We have used published results to calculate the X-ray fluxes expected from moderate auroras as well as the anticipated background fluxes which arise principally from the solar albedo. These numbers are derived only for the purpose of establishing the approximate level of expected counting rates. Unfortunately, the reduced funding level did not permit us to do a more detailed calculation of the spectra and fluxes as a function of source and detector geometries. The discussion of expected auroral and background fluxes is presented in Sections 3 and 4.

The feasibility of flying the auroral X-ray telescope (AXT) leads to an important requirement for the supporting spacecraft, namely, the use of a despun platform from which the telescope can be pointed. While this requirement is a general one for imaging systems, it is particularly necessary in this case in which low fluxes dictate as high a duty cycle for the observations as possible.

At AS&E we feel that the AXT can open a new frontier in auroral research. With the AXT, X-ray aurorae can be detected on the dayside and nightside hemispheres. X-rays can be used for quantitative study of the mid-latitude dayside aurorae, which occur only during very large magnetic disturbances and are difficult to detect optically. Daytime and nighttime injection can be studied at any time of the year without interference from sunlight, the moon, or clouds. The X-ray fluxes and spectra can be used to unfold the spectrum of the incident energetic electrons, a result which can not be obtained from optical data.

The potential for discovery in X-ray pictures of the earth should not be underrated. Apollo mission photographs of the earth, DMSP

mosaics of the auroral zones and Skylab solar images have transformed astrogeophysics. Images of X-ray emission of the earth may similarly transform magnetospheric physics.

2.0   THE TELESCOPE OPTICAL DESIGN

2.1   Design Considerations

Several factors must be considered in the design of an X-ray
telescope. The parameters of a Wolter grazing incidence telescope
that we considered are: f, focal length; Ac, collecting area; Ap,
polished surface area; R, mirror radius; S, mirror segment length;
α, angle of incidence between the mirror surface and an incoming
ray parallel to the optical axis; ρ, the spatial resolution; FOV,
field of view; λ, wavelength; λc the short wavelength cutoff; and
NN, the number of nested coaxial, confocal mirrors.

The most important factors for the AXT design are:

(1) Large Ac. The low flux levels discussed in Section 3 make
     this a particularly important criterion in order to get
     reasonable counting rates. If f is fixed, this is generally
     achieved by increasing R and S. If R is fixed, one decreases
     f, at the price of lengthening the short wavelength cutoff
     λc. Increasing S and NN also increases Ac.

(2) Moderate ρ. Solar and stellar telescopes have achieved a
     resolution of 2 arc sec, but this is well below the
     characteristic scale of the auroral features to be studied
     from a spacecraft at ~ 10 R_e. In addition, the low flux
     levels would not allow a high spatial resolution to be
     effectively utilized, since the number of photons per pixel
     per unit time would become vanishingly small.

(3) Modest f. Since the size of the image in the focal plane is
     proportional to f, and, as we discussed above, ρ can be
     moderate, this implies that f can be shorter on AXT than on
     solar instruments such as Skylab (213 cm) and the Inter-
     national Solar Polar Mission (83 cm) or stellar instruments
     such as the Einstein Observatory telescope (340 cm).

(4) Appropriate λ response. As the ratio R/f increases, α increases. As that angle increases, the short wavelength cutoff, λc, increases. Care must be taken that λc stays below about 10 A so that the wavelength range of interest can be studied.

(5) Large FOV. Since the angular size of the auroral region to be studied exceeds the usual 1 - 2° field of view of a grazing incidence telescope, the design chosen for the AXT should incorporate as large a FOV as possible. A corollary to this requirement is the additional requirement that the spatial resolution ρ should be moderately good over the entire field of view accessible to the CCD. Since ρ deteriorates with increasing angular separation from the optical axis, and only a moderate on-axis ρ is required (see point (2) above), designs optimum in other respects may have an unacceptably poor ρ near the edge of the FOV.

(6) High ratio of Ac/Ap. The cost of telescope mirrors scales roughly in proportion to Ap, so a high ratio Ac/Ap means a high ratio of collecting area to cost. This requirement obviously couples to (1) and (3) since a high Ac/Ap is best achieved by a large ratio of R/f for wavelengths above λc.

(7) Small focal plane image. The image size must be no greater than that of typical CCD's. The RCA CCD has dimensions of 7.3 mm by 9.3 mm. This requirement must be considered in conjunction with (3) and (5) above.

Although many trade-offs can be performed in selecting an optical telescope design, as we have seen above, the last requirement (7) is paramount in driving the design. If one wishes to image the entire auroral zone of angular size θ on the CCD, the focal length is determined by $f = d/\theta$, where d is the dimension of the CCD.

For a satellite such as the PPL at 15 R_e, a FOV of 0.65 R_e, necessary to see the entire auroral zone, yields a required f of 16.8 cm or less if the auroral zone is to be imaged on the RCA CCD. We calculated the properties of a set of nested mirrors with NN = 6 and f = 10 cm through a computer ray tracing program. An α = 3.5° allowed the largest reasonable R of 2.44 cm without serious loss of sensitivity at λ = 19 A. The result was that the on-axis Ac was only 3.5 cm^2, inadequate to provide the level of counting rates needed to make the experiment viable (see Section 3 for a discussion of counting rates). This result then forced us to consider imaging the auroral zone in quadrants, i.e., four images making up the entire zone. This relaxes the focal length requirement to f = 35 cm.

From this point on, we examined only f = 35 cm designs. In order to maximize Ac, we increased R until α reached ~ 3.5°, at which point Ac at 23.6 A peaks and begins to decline. In past designs we have found that letting S = 2 R results in a mirror design with a reasonable tradeoff between a large Ac, which increases linearly with S, and a small ρ, which also increases with S.

2.2 Wolter vs. Baez Designs

We let NN = 7, which is only one mirror less than the maximum feasible number for a reasonable assumed mirror thickness. Table 2-1 lists the properties of each of the individual concentric, confocal mirrors. The mirror surface is nickel, which provides a high reflectivity in the wavelength range of interest. An alternative surface, gold, is a better reflector at short (<10 A) wavelengths, but nickel is better at the longer wavelengths used here.

Designs for a Baez telescope were also examined. The Baez optical elements have the advantage of being relatively cheap to fabricate and should be considered as a possible alternative to the Wolter

Table 2-1.

Mirror Efficiencies

Focal length = 35.0 cm Paraboloid length = 18.08 cm

Hyperboloid length = 11.92 cm Mirror thickness = 3.5 mm

Mirror Number	α (degrees)	Central Radius (cm)	Effective Area (cm^2)			Mirror Utilization Efficiency at 23.6 Å (percent)
			at 8.34 Å	at 23.6 Å	at 31.6 Å	
1	3.70	9.04	0.01	18.4	24.6	3.69
2	3.10	7.57	0.05	18.6	21.0	4.45
3	2.56	6.26	0.29	16.0	16.9	4.62
4	2.09	5.11	1.35	12.5	12.8	4.43
5	1.67	4.08	2.78	9.0	9.1	3.98
6	1.29	3.16	2.96	6.0	6.0	3.41
7	0.96	2.34	2.29	3.6	3.6	2.75
8	0.66	1.62	1.37	1.8	1.8	2.04

design. We compared two telescope designs, holding the focal
length and the maximum grazing angle the same for each for the
reasons discussed above. The values used were 35 cm and 3.7° for
the focal length and maximum grazing angle, respectively. A major
difference between the two designs is that in the Wolter design
the radius $R = 4\alpha f$, while in the Baez design $R = 2\alpha f$. This is
due to the fact that in the Baez design the first set of mirrors
reflects all rays incident from a point source by an angle 2α onto
a line image in the focal plane. The second set of mirrors
reflects the rays by 2α in a plane perpendicular to that of the
first mirrors. This differs from the Wolter telescope, in which
each incoming ray is reflected by a total angle of 4α to the
focal plane. The result is that the diameter of the mirrors is
twice as large in a Wolter design as in a Baez design for the same
focal length. The Wolter nested set therefore has a larger
collecting area by at least a factor of R^2, or about 4.

In the two competing designs the mirror segment lengths were fixed
at 18.08 cm and the focal lengths were kept fixed at 35 cm. The
maximum reflection angle α was 3.7° for each. Seven nested
mirrors were used in the Wolter design. The Baez design program
uses the largest number of mirrors that can be fitted into the
available aperture. A nickel surface was used for both designs.

The resulting calculated areas and blur circle radii are plotted
in Figures 2-1 and 2-2. The Wolter design has a collecting area
larger by a factor of about 8. The Wolter blur circle radius is
better for the inner part of the FOV and inferior to the Baez
design over the outer part of the AXT FOV. Overall, the spatial
resolutions of the two designs are comparable, but the superior
collecting area of the Wolter design dictates its selection as the
optimum design for the AXT. Characteristics of the seven nested
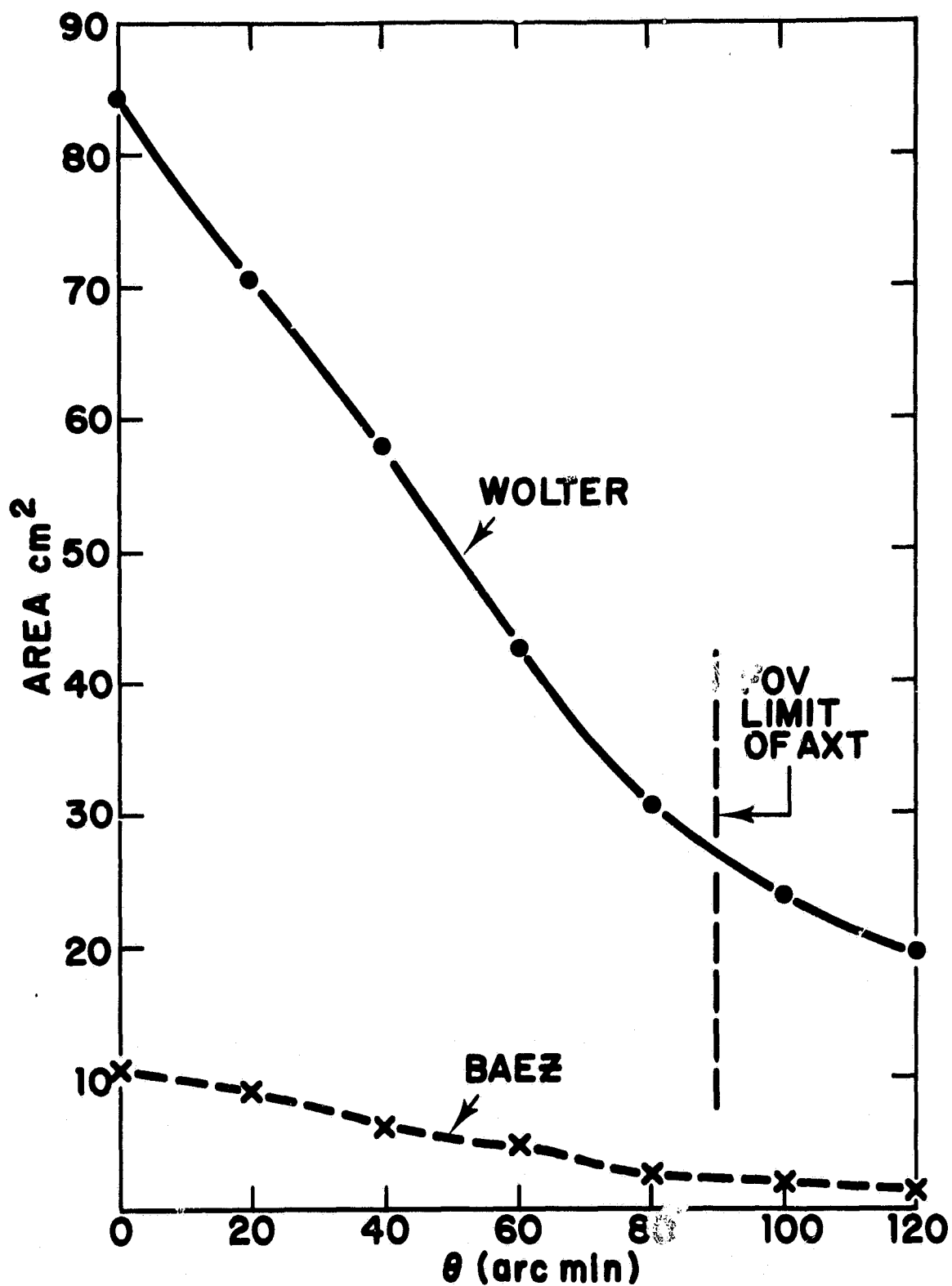mirrors of the AXT are shown in Table 2-1.

Figure 2-1. Effective collecting area of Wolter and Baez mirror
arrays for 19Å X-rays as a function of angular
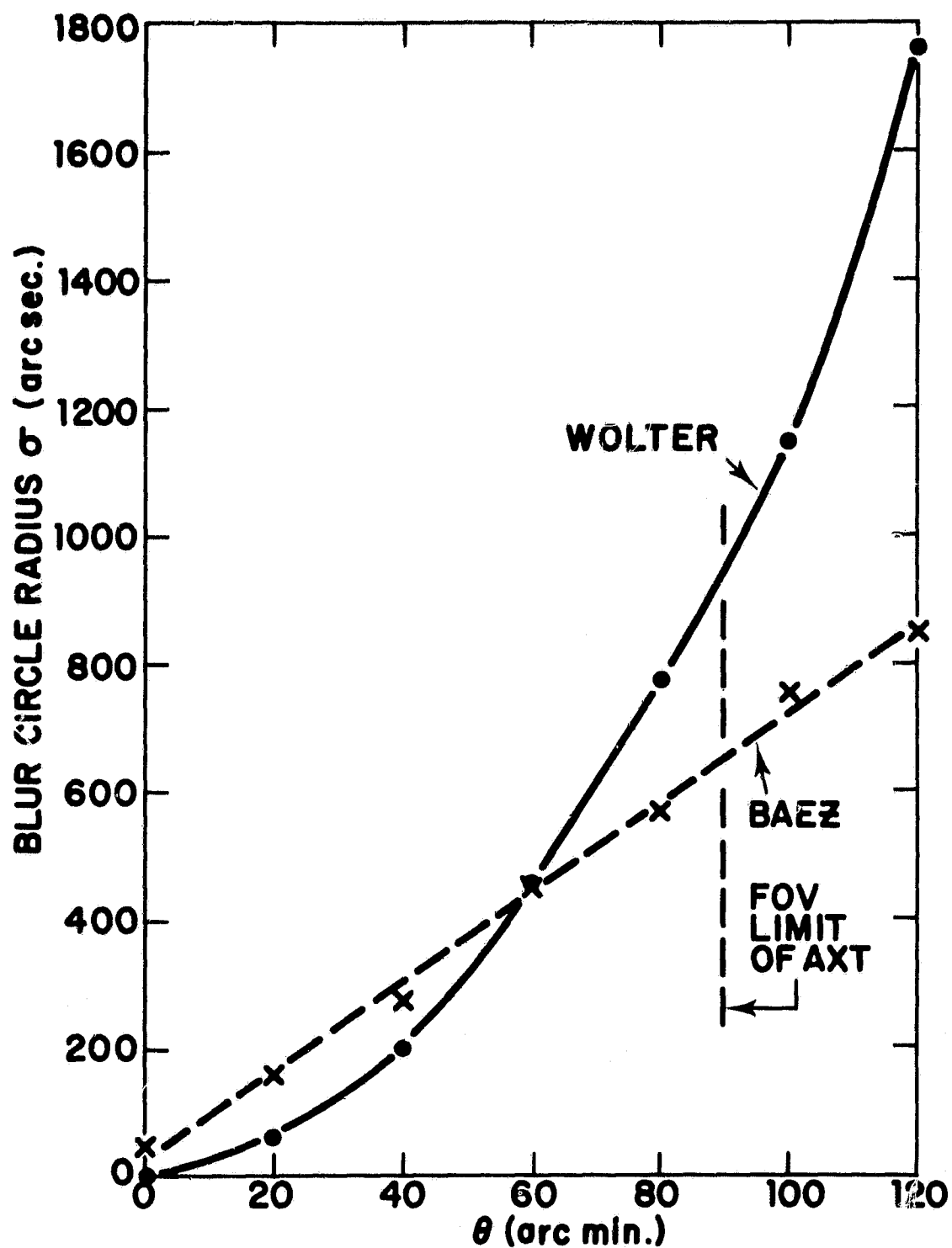distance from the optical axis.

Figure 2-2.   Blur circle radius for Wolter and Baez mirror arrays
as a function of angular distance from the optical
axis.

2.3   Mechanical Design of Mirror Assembly

2.3.1   Introduction

The basic mirror assembly is based on the grazing incidence Wolter Type I mirror with a nest of 7 hyperboloid/paraboloid mirror sets. The mirror assembly is 25 cm. in diameter and 35 cm. long, with a focal length of 35 cm. A sketch showing the main components of the mirror assembly is shown in Figure 2-3.

Our studies considered the traditional structural problems associated with mirror designs. We sought to achieve a very high collecting area and to support the optics with minimum distortion. Distortions can be drastically reduced by thickening mirror walls and the center support plate. These measures, however, reduce the collecting area of the telescope. The mirror must be designed to keep the distortion within allowable limits while maximizing collecting area.

Since the mirror assembly will be fabricated, assembled, tested, and calibrated in a 1-g field (i.e. on earth), gravity will distort the optic and the mirror assembly, to some extent adversely affecting the overall resolution of the system. On past programs AS&E has been successful in calibrating out the effects of gravity. The procedure increases the cost of assembly but reduces the error to the limit of the measuring technique, which has an accuracy of a few arc sec.

Distortions due to the thermal environment are a major concern. When the mirror assembly is operational in orbit, its thermal environment is constantly changing. Although the temperature can be controlled by active or passive systems, the mirrors can never be held isothermal at their assembly temperature. As the system undergoes thermal excursions, discontinuities occur at the interfaces of materials with differing coefficients of thermal
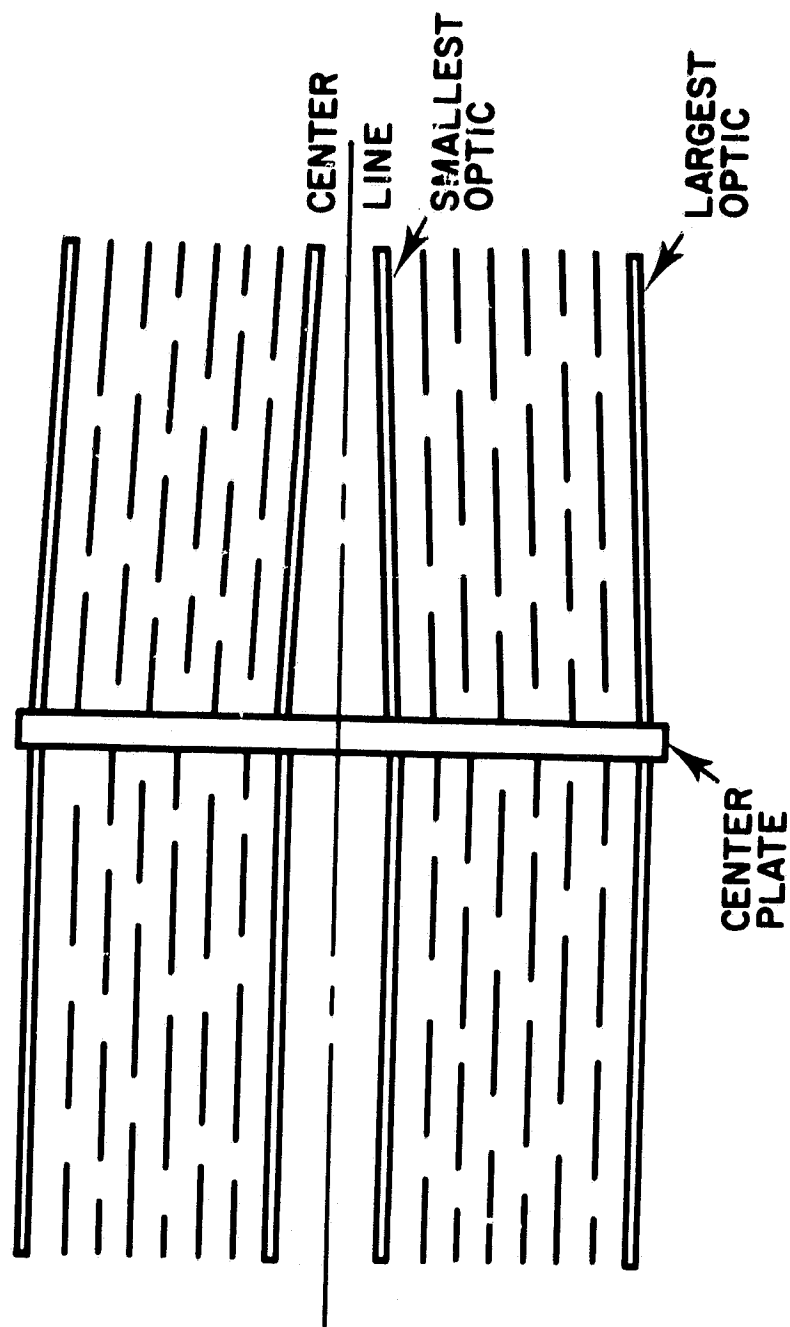
Figure 2-3. Mirror Assembly Schematics.

Labels in figure: CENTER LINE, SMALLEST OPTIC, LARGEST OPTIC, CENTER PLATE

expansion. The loads occurring at these discontinuities distort the system and induce figure errors on the surfaces of the mirrors. The effects of these loads must be considered in the error budget. One should try to select materials with matching coefficients of thermal expansion to yield the smallest loads and thus, the least sensitivity to thermal soaks,

Thermal gradients set up in the mirrors and optical bench also distort the optical surface, degrading resolution. An assessment of this effect was made in order to determine the required thermal control.

The launch and pre-launch environment pose additional constraints on the design. Regardless of impact on resolution, weight or collecting area, the mirror assembly must be designed to withstand the rigors of possible large temperature swings (85°C) and high vibration environments (60g) at launch.

There will be non-environmental errors due to limitations in fabrication and assembly techniques. The mirrors will have a finite blur circle associated with figure errors and surface roughness. In past programs, we have controlled these factors to more stringent requirements than imposed by the AXT program. The allowed blur circles indicate that a relative reduction in mirror costs will be possible.

2.3.2 Design Objectives

General

The most general design objective is the minimization of cost. The design should be as simple as possible to manufacture and assemble while still meeting the performance requirements. The raw materials should be cheap and easy to machine, such as aluminum or steel. Expensive composite materials, such as

graphite/epoxy or beryllium and titanium, which have unique properties yielding performance not attainable otherwise, should be used only where performance dictates.

Weight should also be minimized. This is common to all space projects where launch weight has a large impact on cost. This would suggest that light materials such as graphite/epoxy or aluminum be used rather than materials such as invar or stainless steel. Already, it can be seen that conflicting objectives exist.

Another general design objective, which also allows the minimization of weight, is to maintain the first resonant frequency above 100 Hz. Since most of the energy in launch is in the form of vibration at frequencies below 100 Hz, all resonant frequencies in the system should be above 100 Hz. This keeps the 'g' loading to a minimum and lowers the requirements for heavy, strengthening materials.

Specific

An important specific design objective is to maximize collecting area. An ideal hyperbola/parabola mirror set, not separated at the interface and not supported by radial ribs, will collect 100% of the incident energy. Since a mirror set cannot be made from one piece of glass, there must be some finite space between the two elements. The minimum space between mirror elements is determined by the thickness of the center plate. Also, since the mirrors must be held in precise alignment, they must be connected by radial ribs, which also cut down on the collecting area. We sought to minimize the obscuration by ribs and the loss of collecting area due to axial separation of the mirrors.

The mirror design goal is a resolution of 10.0 arc-seconds. This means that the mirror should be able to differentiate between two X-ray point sources separated by a minimum of 10.0 arc-seconds.

If the mirror optical elements were perfect, the optical assembly
would focus on-axis rays at a diffraction-limited point, and,
therefore, be able to resolve two X-ray sources separated by an
almost infinitesimal amount. Factors which degrade resolution are
figure and surface errors, assembly errors, and environmental
effects. The result of all these factors is that the mirrors do
not focus at a point, but rather in an area considerably larger
than the diffraction limit. We assume that a scan across this
area would yield a normal Gaussian distribution of energy. If the
distribution is truly normal, the resolution of the mirror is
defined as the size of the circle in which 67% of all energy lies.

2.3.3   Analysis

Analysis was carried out for four areas: launch environment,
gravity deformations, thermal deformations, and fabrication
errors. Error allocations for each area were prepared and used as
design goals for individual elements of the analysis. The error
budget is shown in Table 2-2.

Surface errors in the mirrors from different sources were
evaluated and combined by root-mean-sum (RMS) and root-sum-of-
squares (RSS) techniques as discussed in Appendix I.

The design constraints and goals are listed in Table 2-3.

2.3.3.1   Extreme Environment Stresses and Dynamic Analysis

Launch Loadings

We analyzed the stresses developed in the system under a 60-g
acceleration loading. A 60-g loading approximates the worst
loading the system may experience during shuttle launch. The
typical random vibration level during launch is on the order of
10.0g RMS. Taking a 3σ level of the RMS value and doubling it to
account for amplification of the input vibration level in the

Table 2-2.
RMS Blur Circle Error Budget

	Blur Circle (=X)	X^2
Fabrication Defects		
Figure & Alignment	4 arc-sec	16
Scattering from Roughness	4 arc-sec	16
Gravity Deformations		
Sag	4 arc-sec	16
Tilt	4 arc-sec	16
Environmental Effects		
Temp. Soak + 5°C	4 arc-sec	16
Temp. Gradients	4 arc-sec	16
	$\Sigma X^2 =$	96

RSS < 10 arc-sec.

Table 2-3.

Structural Constraints and Goals

Weight	31 kg max
Geometric Collecting Area	93% of total circular area
Dynamic Resonances	100 Hz min
Stresses	P.E.L. Be = 8 Ksi Max
	Ti = 70 Ksi Max
Optical Resolution	10 arc-seconds

system gives the 60-g level. Safe stress levels for most materials were established as those which show factors of safety of at least 1.25 on the yield stress and 1.5 on the ultimate stress. For materials where it was felt that permanent offset would degrade the resolution of the system, the Precision Elastic Limit (P.E.L.) was used. P.E.L. corresponds to 1 micro-inch/inch permanent offset. A summary of stresses in the center plate vs. plate thickness is given in Table 2-4.

Our dynamic studies investigated the predominant modes of vibration in the system with the purpose of identifying any natural frequencies below 100 Hz for reasons discussed in Section 2.3.2. We investigated the predominant modes of the mirror assembly only and not of the mirror assembly as it interacts with the rest of the instrument. A summary of the investigation into two of the modes of vibration is given in Tables 2-5 and 2-6. The modes of distortion are shown in Figures 2-4 and 2-5.

85°C Thermal Swing

We analyzed the stresses developed due to coefficient of thermal expansion (C.T.E.) mismatch during extreme temperature conditions. In particular, we investigated the effect of 85°C thermal swings on the acceptable stress levels:

Center Plate Thickness	Stress in Large Optic	F.O.S.*	Stress in Small Optic	F.O.S.
1.9 cm Be	133 psi	60.21	1014 psi	7.89
0.76 cm Ti	7323	1.09	10995	.73

We conclude that a titanium centerplate will be entirely unacceptable because of the very great stress due to the thermal mismatch between the optics and the centerplate.

---

*Factor of Safety
 (= acceptable stress/actual stress)

Table 2-4.

Stresses in the Center Plate

- 60g assumed max. shuttle launch load
- Beryllium P.E.L. = 8 ksi
- Titanium P.E.L. = 70 ksi

Stresses Due to Loading Along the Mirror Axis

Center Plate Thickness (cm)	Stress in ksi		Factor of Safety Beryllium	Titanium
0.50	84.8 ksi		0.09	0.83
0.65	67.8 ksi		0.12	1.04
0.80	43.2		0.19	1.62
1.00	29.3	not acceptable	0.27	2.39
1.27	16.9		0.47	4.14
1.90	7.6	acceptable	1.05	9.21
2.50	4.2		1.90	16.67

Figure 2-4. Vibrational Modes in a Mirror Set.

MIRROR

DEFORMED SHAPE OF MIRROR

DEFORMED SHAPE OF CENTER PLATE

CENTER PLATE
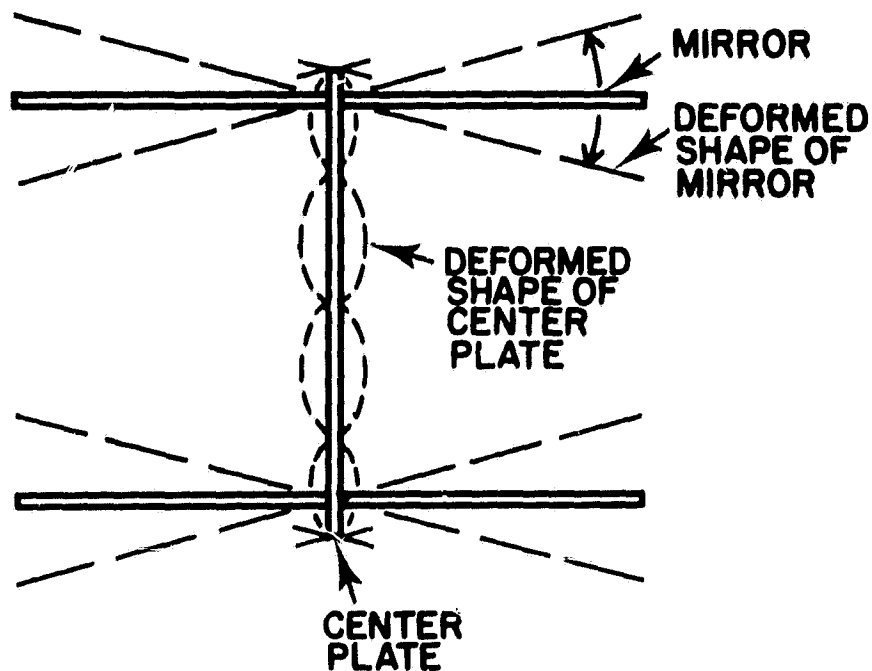
Table 2-5.

Mirror Assembly Minimum Resonant Frequencies
(Design Goal > 100 Hz)

	t	Be	Ti		t	Be	Ti
Small Optic	2.5	12 Hz	8 Hz	Large Optic	2.5	211 Hz	130 Hz
	7.6	64	39		7.6	1100	693
	12.5	137	84		12.5	2360	1448
	17.8	228	139		17.8	3920	2398

acceptable

t = thickness of center plate (mm)

Table 2-6.

Center Plate Minimum Resonant Frequencies
(Design Goal > 100 Hz)

Frequency (Design Goal is f_n = 100 Hz)

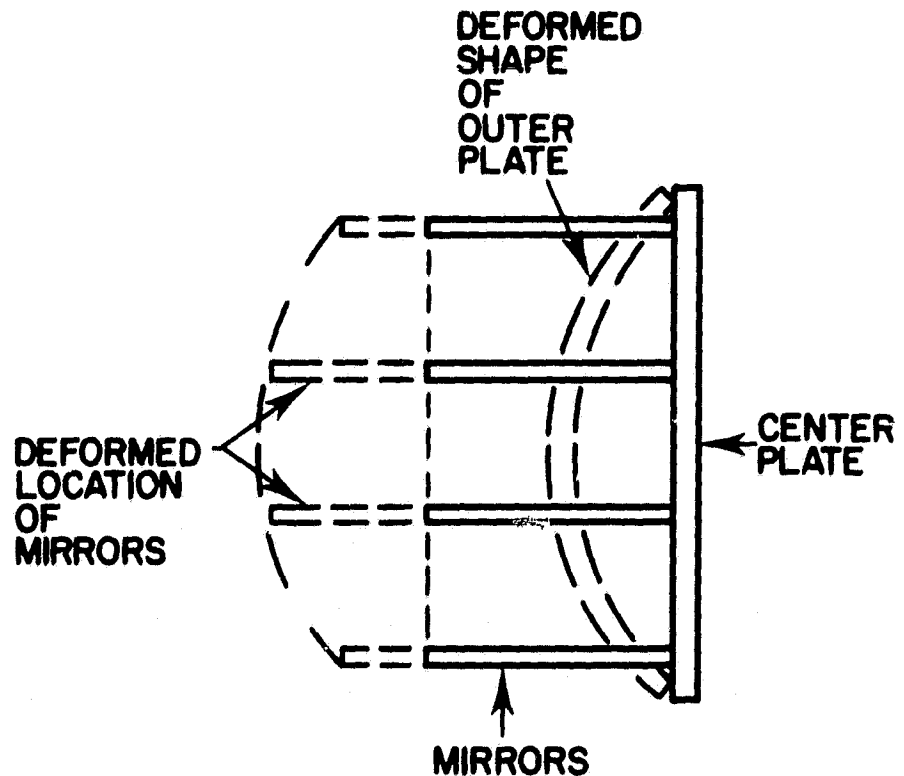| Center Plate Material	0.3	Center Plate Thickness (cm)				
		0.5	0.65	0.80	1.0	1.27
Beryllium	81 Hz	174	243	341	456	688
Titanium	50	107	149	209	279	421

Acceptable

Figure 2-5. Dynamic Distortion of the Center Plate.

2.3.3.2 Gravity Deformations

The deformation of the mirror is a combination of two effects:
first, beam action, i.e., mirror bending and shearing due to the
way the mirror is supported at the end. Deformations are observed
at the sides of the mirror or at the $\theta = 90°$ meridian in our
computer model. The $\theta = 0°$ meridian is longitudinal along the top
of the mirror. The mirrors are cantilevered off the center plate
via flanges, while held on the ends by an aperture plate and
support cylinder. The beam bending and shear characteristics
produce, in the first approximation, an angle between the two
mirrors at each set. This angle produces an image defect similar
to coma except that a point source is imaged into a ring.

The second deformation occurs when a segment sags under its own
weight as a ring, where the circular cross section takes on an egg
shape. This effect shows up primarily at the top and bottom of
the mirror, or along the $\theta = 0°$ meridian in the model. The result
is an image blur proportional to the RMS figure error.

The two gravity distortions and the images each produce are
sketched in Figure 2-6.

A quantitative assessment of the two modes of gravity distortion
showed that a 1-g sag results in a 0.022 arcsec blur circle. A
1-g tilt causes a 0.016 arcsec blur circle for the largest mirror
and a 0.16 arcsec blur circle for the smallest mirror.

2.3.3.3 Thermal Deformations and Effect on Resolution

As pointed out in the discussion of extreme environments, the
C.T.E. mismatch in the mirror and mirror mount will produce
stresses and therefore distortions in the mirror. We analyzed the
resultant distortions in terms of the RMS figure error. Its
effect was then related to blur circle and resolution.

1-g SAG, TILT, AND BIAS

● SAG   IMAGE
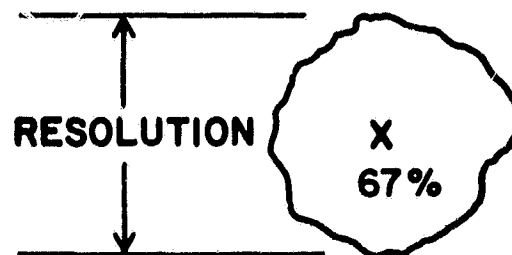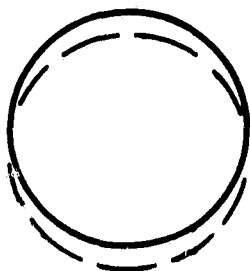
● TILT

Figure 2-6. Mirror Deformations for 1-g Sag and Tilt.

±5° Soak Temperature

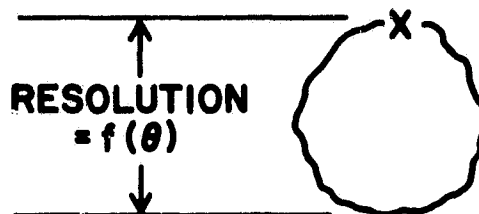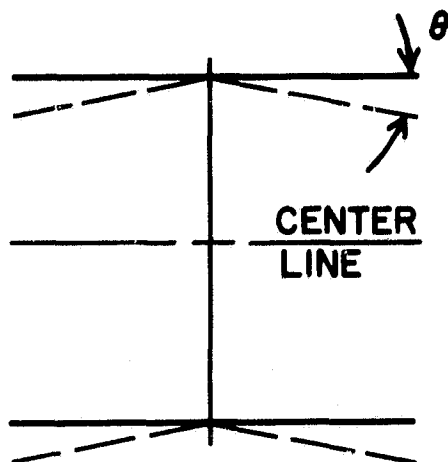The expansion difference between the center plate and the mirrors was analyzed for its effect in the RMS slope error of the mirrors. Each of the seven mirrors was analyzed. The results were combined by weighting the distortions in each mirror by its collecting area. Results of this analysis are summarized in Table 2-7.

Thermal Gradients

We analyzed the effects of gradients along the length of the mirror package and across the sides (i.e. side-to-side, top-to-bottom) of the package. The results, summarized in Table 2-7, show a much greater sensitivity of mirror resolution to side-to-side gradients than to end to end gradients.

Due to symmetry in the mirror package, it will be easier to maintain a tighter side-to-side gradient than end-to-end gradient. A side-to-side gradient of 0.5°C and an end-to-end gradient of 2°C are generous when compared to past experiments and will not require any advances in thermal control.

2.3.3.4   Fabrication and Alignment Errors and Effect on Resolution

Figure and Alignment

This budget is set for 4 arc-sec considering that 1 arc-sec has been achieved for other programs. This should afford a considerable relaxation in quality procedures. The results can be easily checked optically.

Surface Roughness

Surface roughness can be treated as an RMS slope error and can thus be combined with other errors in the RSS manner. The allocated budget of 4.0 arc-sec is generous when compared to past programs and should allow cost savings.

Table 2-7.

Thermal Effects on Resolution

- Resolution Effects Due to ±5°C Thermal Swing

| | Center Plate Material | |
	1.9 cm Beryllium	0.76 cm Titanium
Largest Optic	0.479 arc-sec	2.86 arc-sec
Smallest Optic	0.110	0.563
RMS Total for Entire Nest	0.352	2.080

- Resolution Effects Due to 1°C Gradient

	Resolution Effect
1° C End-to-End Gradient	0.418 arc-sec
1° C Side-to-Side Gradient	6.282

2.3.4   Summary

The 10 arc-sec resolution goal of the mirror system has to be treated as dependent on a combination of many effects: environmental, manufacturing, and assembly. Our analysis has shown the extent of environmental effects. Previous experience has helped us set the achievable budgets for fabrication and assembly.

An evaluation of a mirror system utilizing a 1.9 cm thick beryllium center plate with allowable thermal limits as follows is given in Table 2-8.

Thermal soak	$T = \pm\ 5°C$
Side to side gradient	$T = \pm\ .5°C$
End to end gradient	$T = \ \ 2°C$

The evaluation shows the 10 arc-sec design goal to be attainable, and it also shows, with the relatively good isolation from environmental effects, that fabrication tolerances can be relaxed.

Table 2-8.

Summary: Effects on Resolution of Various Error Sources

Effect	Budget	Achieved
Fabrication Defects		
Figure and Alignment	4. arc-sec	4. arc-sec
Roughness	4.	4.
Gravity Deformations		
Sag	2.	0.022
Tilt	4.	0.056
Thermal Effects		
5° C Soak	4.	0.352
0.5° C S-S gradient	4.	3.141
2° C E-E gradient		0.836
RSS	10. arc-sec	6.64 arc-sec

3.0 EXPECTED AURORAL X-RAY FLUXES

3.1 Auroral Emissions

On the basis of observations by Mizera et al. (1978) and the theoretical work of Luhmann and Blake (1977), we can estimate the count rates expected for various auroras. Since the aurora is an extended source, that is, each pixel of the detector is fully illuminated by auroral structure, we may compute the flux F on one pixel as follows:

$$F = A(\lambda)I \frac{d^2}{f^2}$$

where $A(\lambda)$ is the effective collecting area of the telescope. $A(\lambda)$ includes the effect of 2000 Å of aluminum prefilters and the response curves of the telescope and CCD. $A(\lambda) \sim 30$ cm^2 at 0.5 keV. I is the X-ray flux in photons cm^{-2} sec^{-1} keV^{-1} sterad^{-1}. We take $I \sim 5 \times 10^5$ photons cm^{-2} sec^{-1} keV^{-1} sterad^{-1} in a moderate aurora.

The pixel dimension d is 30×10^{-4} cm and the telescope focal length is 35 cm. We estimate the count rate in 170 eV bands at ~0.5 counts per second per "macropixel," which is a 4 x 4 block of pixels averaged during readout of the CCD. The above estimate applies to moderate aurorae which occur about 10 days per month. Brighter aurorae, with 10 times this flux, are not uncommon.

Readout can be accomplished with approximately the same amplifier noise for each 16-pixel block that holds for single pixels. Only the dark current noise increases, but it is negligible (less than one electron per second at –60°C). A readout rate of 0.25 seconds will help keep the number of two photon events low without causing excessive pulse height spreading near zero signal.

Basing our calculations on a moderate aurora, we find that 400 integrations (100 seconds) should yield 40 counts in the K_α lines of oxygen and nitrogen, which are so close together that they cannot be resolved with a CCD detector. Longer exposures or larger macropixels will be required to obtain three-sigma count levels at 1 - 3 keV. We expect that integration times will vary between 10 seconds over the brightest auroras and 1000 seconds, or more, in faint auroras. Integration times could be determined either by explicit command sequences, or by the total signal level, as recorded continuously in a separate register. During periods of bright aurora, the total signal level can be used to trigger a drop in the integration time. This feature should be included because the brightest features also are the most rapidly changing.

3.2 Expected Pulse-Height Distribution

We have modeled the total response of the AXT to theoretical X-ray spectra in order to illustrate the expected count rates, readout noise and pulse height spreading. If no more than one photon interacts in a pixel in each 0.25 sec sample interval, the distribution over many interactions is a differential photon number spectrum, $dN(E)/dE$. The transmission of any filter, $F(E)$, the mirror area, A, and reflecting efficiency, $\varepsilon_M(E)$, and the detector efficiency, $\varepsilon_D(E)$, must all be accounted for. All that remains is to convolve the CCD spectral resolution $G(E,E")$ with the detected spectrum to find the resultant pulse height distribution, $n(E)$, which is expressed in counts per pulse height bin:

$$n(E_l, E_u) = \int_{E_l}^{E_u} \int G(E,E") \int \frac{dN(E')}{dE} F(E')A\varepsilon_M(E')\varepsilon_M(E')\varepsilon_D(E')dE'dE"dE$$

where E_u and E_l are the upper and lower edges of the energy bin under consideration.

We have selected 0.25 seconds as the nominal base sampling period. This allows sufficient distance between the zero energy peak and the K-lines peak to separate the two reliably. At the same time, the rate of accidentals (two or more photons during one sample interval) is low enough so as not to mask the less intense regions of the spectrum.

In Figure 3-1 we show the expected response of our instrument to two X-ray spectra from idealized electron beams with α of 1 and 15 (α is the index of spectral hardness). Also shown is the AXT response to the Frank and Ackerson electron spectrum analyzed by Luhmann and Blake. We estimate that $\alpha = 8$ in this case. While the K_α lines dominate the spectra, it is clear that the 1 - 3 keV response will allow one to differentiate among these spectra. Time integrals of 100 - 1000 seconds over this band easily yield > 3σ results.

On the dark side of the earth, the minimum detectable flux (3σ) is of the order of 10^4 photons sec^{-1} cm^{-2} sec^{-1} keV^{-1} $sterad^{-1}$ (including the K_α-lines) over a time scale of ~ 1000 seconds. The dayside minimum is higher because of the earth's solar X-ray albedo, as described below.

For any moderate aurora the AXT can give a reliable estimate of the index of the electron spectrum and the total electron energy. In general, the strength of the K_α lines relative to the continuum will yield information on the proton/electron ratio for any event.

3.3   Interpretation of X-Ray Spectra

Auroral X-ray emission spectra above 1.5 keV have been measured and found to be in good agreement with the bremsstrahlung expected from electron impact regions in the auroral atmosphere (Mizera et al., 1978). Below 1.5 keV, auroral X-ray emission is bremsstrah-
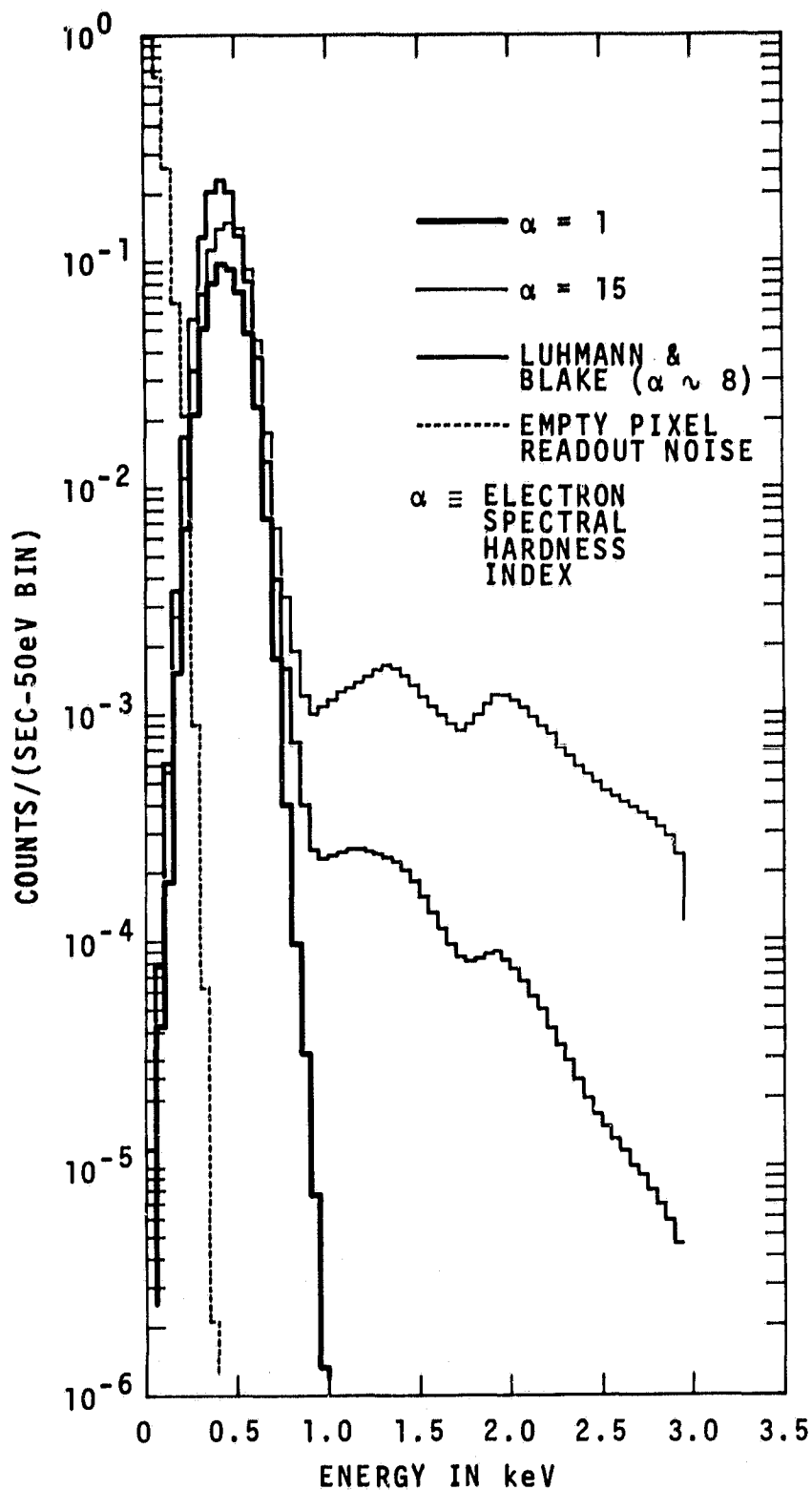
Fig. 3-1. Expected pulse height distribution for various input spectra. The total AXT response including telescope and filter transmission curves has been taken into account. Detector response and pulse height spreading are also included.

3-4

lung plus K_α line emission from nitrogen and oxygen (Luhmann and Blake, 1977). The flux in 170 eV intervals containing these lines is more than ten times that from electron bremsstrahlung. While electron bremsstrahlung will always accompany the K_α line emission in the X-ray spectra of electron aurorae, the bremsstrahlung from a pure proton aurora would be negligible. An X-ray instrument with an energy resolution of 170 eV would be able to discriminate between electron aurorae and proton aurorae. In Section 5, we discuss the progress being made in production of CCD's capable of 170 eV energy resolution at X-ray energies.

Detailed interpretation of the measured bremsstrahlung and K_α emission depends on knowledge of the relationship between the X-ray spectra emerging from the top of the atmosphere and the precipitating particle spectra. Aspects of this relationship have been explored by a number of authors (Luhmann, 1977; Luhmann and Blake, 1977; Seltzer and Berger, 1974). However, this area should be further explored in a program of analytical and Monte Carlo calculations which take into account: (a) the penetration, energy degradation and angular diffusion of the incident electrons or protons, (b) the production of bremsstrahlung or K_α X-rays, and (c) the escape of these X-rays from the top of the atmosphere. These studies should use the best available data on the stopping power and range of electrons and protons, bremsstrahlung production cross sections, K_α ionization cross sections, and photon interaction cross sections for the constituents of the upper atmosphere. Included in the studies should be estimates of the effects of different source and detection geometries, and of the anticipated background level of K_α emission from the atmosphere due to excitation by solar X-rays.

The above studies are recommended to assure that no important physical processes are overlooked in interpreting the auroral X-radiation. Nevertheless, it is already clear that X-rays provide

a more direct link to the primary particles than do optical
emissions. X-rays from aurorae are easier to interpret than
optical or UV emissions. The X-rays are generated by the primary
precipitating electrons themselves, while optical and UV line
emissions result primarily from secondary electron interactions
with many atomic and molecular species distributed in a variable
and sometimes poorly understood way along the precipitation
path. Figure 3-2 contrasts the steps that must be followed to
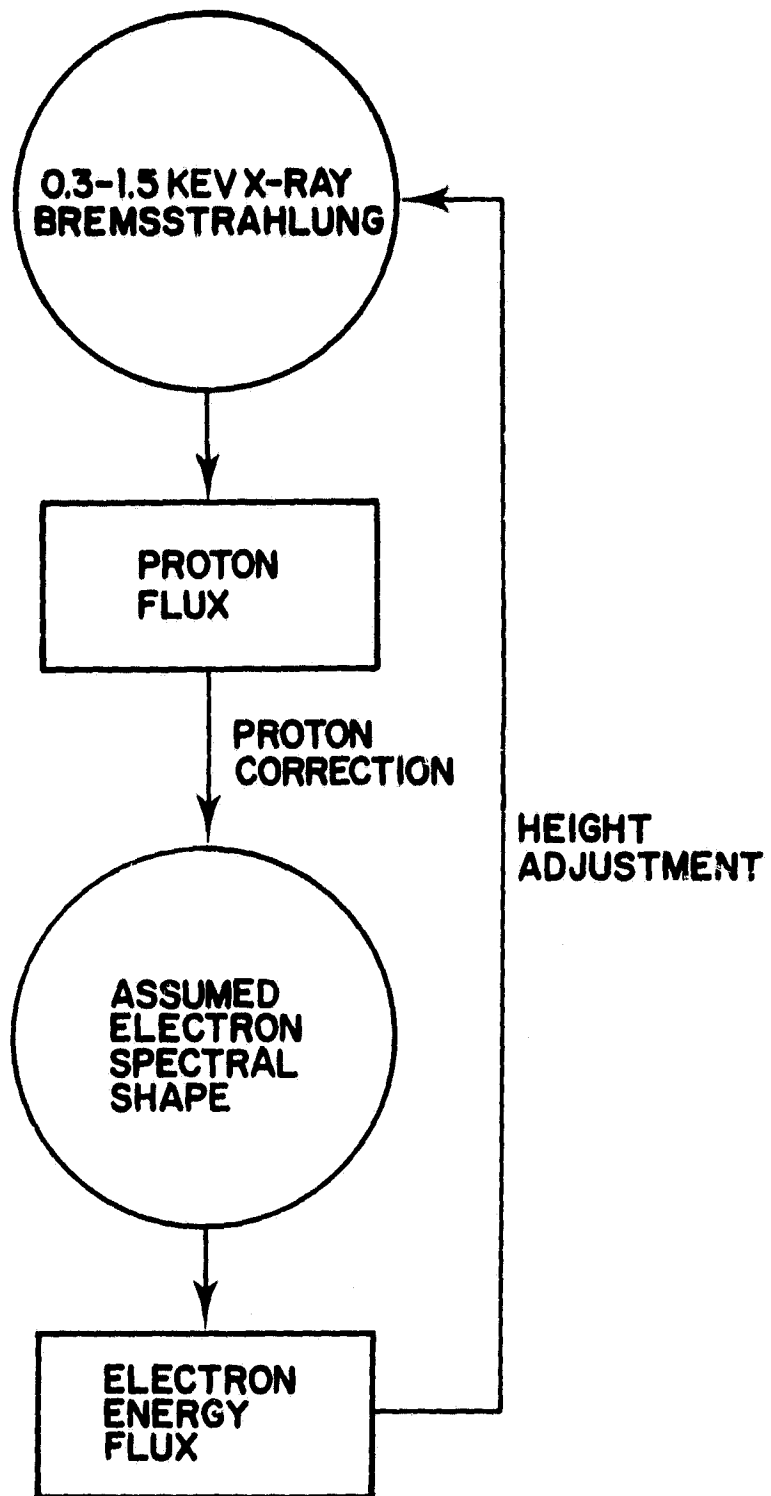interpret X-rays and optical radiation from aurorae.

Figure 3-2a. Schematic plan for applying measurements of auroral X-ray emission to estimate precipitating electron fluxes
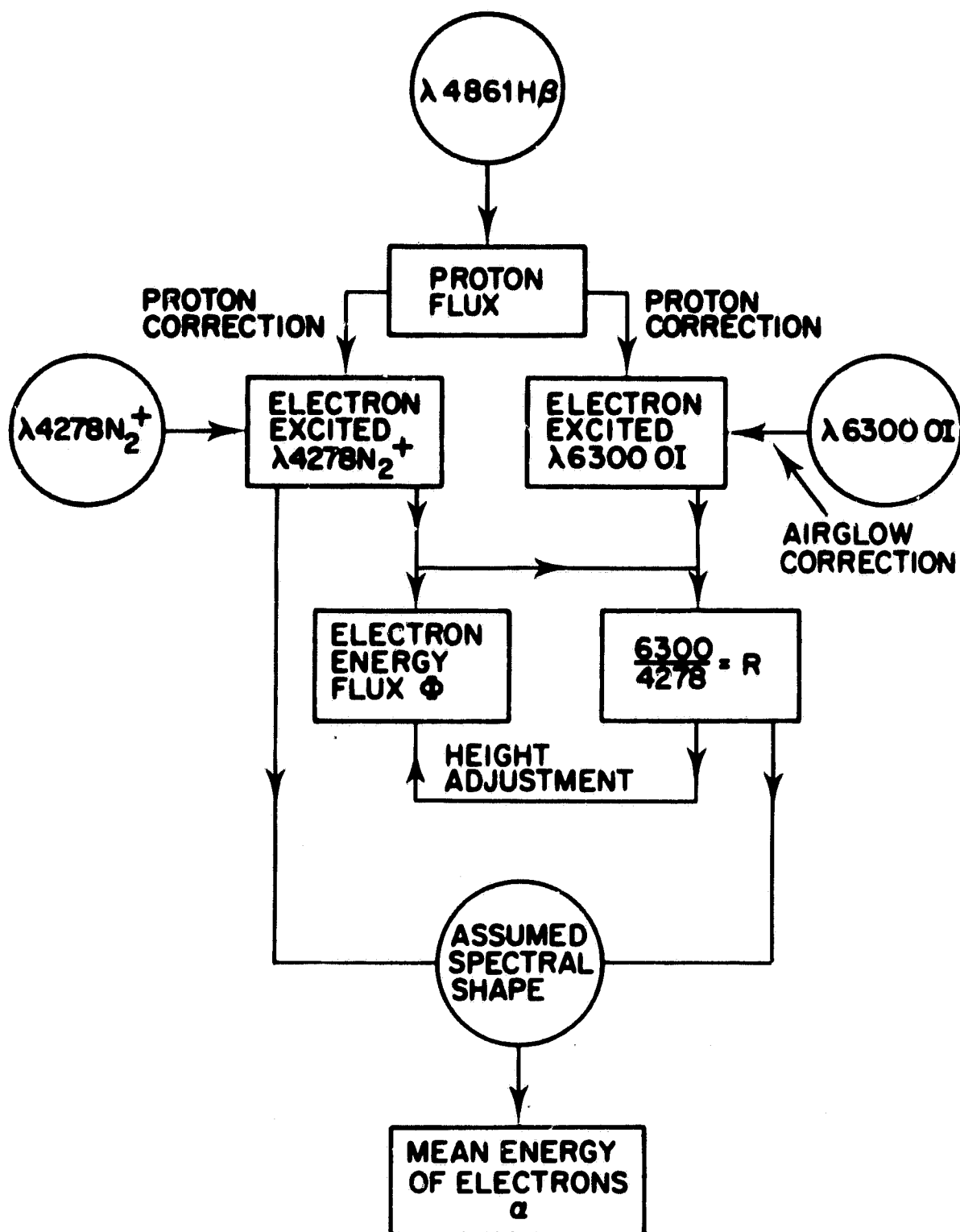
Figure 3-2b. Schematic plan for using optical data to study precipitating electron fluxes. Uncertanties are considerably greater than in the X-ray-based approach.

4.0 SOURCES OF NOISE IN AURORAL X-RAY IMAGES

In this section we investigate the sources of noise which can compromise the auroral X-ray images. These sources can be separated into two broad categories, X-ray and non-X-ray background.

4.1 X-Ray Background

X-ray noise is contamination from non-auroral sources which either mask or overwhelm the auroral X-rays. These X-ray sources are:

- solar X-rays scattered or reflected from the atmosphere,
- cosmic ray induced X-rays in the upper atmosphere, and
- celestial X-rays scattered from the atmosphere.

The optimal observations for sorting out the magnitudes of the various sources of X-ray background are those of Rugge et al. (1978) using the A2 X-ray experiment on the HEAO-1 satellite. They reported observations of the earth's atmosphere with a low energy detector (LED) sensistive in the range of 0.15 < E < 3 keV. Since the HEAO-1 orbit was inclined 23° to the equatorial plane, with an altitude of 425 to 450 km, the auroral zones were not observed. Luhmann et al. (1979) generally found that fluxes from the dark earth matched those from the diffuse galactic background. In several cases they found evidence of nightside atmospheric emission which they attributed to electron precipitation. In each case the atmospheric flux was less intense than the scattered solar X-ray flux observed by Rugge et al. (1978). Those authors published an energy spectrum of the solar albedo with a rather flat flux profile of ~1 photon/cm^2 sec keV in the range of 0.2 to 0.7 keV. Allowing a factor of 5 for the detector efficiency, this results in a flux of ~2 x 10^3 photon/cm^2 sec keV sr, which is lower by a factor of 200 than the estimated flux of a moderate aurora of 5 x 10^5 photon/cm^2 sec keV sr given in Section 3. The

albedo flux will increase in proportion to any flaring increase in
the solar X-ray fluxes, so during times of large flares the albedo
may match or exceed the moderate auroral flux.

4.2   The Non-X-Ray Background

In general, non-X-ray background is not a problem for imaging
detectors. For the CCD, the largest source of background will be
the quasi-Poisson pulse-height distribution associated with
reading empty pixels, as shown in Figure 3-1.

The main source of non-X-ray background will be charged particles
interacting in the detector. Cosmic rays and magnetospheric
positively charged particles are negligible. The only source
which invites deeper inquiry is the electron flux.

In the telescope design discussed in Section 6, electrons can take
no paths to the CCD without passing through some part of the
instrument. The only paths of consequence are those which pass
through the thin aluminum foils (2000 Å). Even electrons that do
penetrate the aluminum prefilters must interact with the mirror
elements or other structures before anything reaches the
detector. We estimate the upper limit to the electron and local
bremsstrahlung flux at ~ 0.1 mimicked photons/sec over the entire
surface of the CCD. During intense electron bombardment, as when
passing through the earth's radiation belts, no data should be
taken.

5.0   CCD DETECTOR RESPONSE TO X-RAYS

5.1   Introduction

We built and tested a soft X-ray imaging camera that uses a
thinned, back-illuminated, all-buried channel RCA CCD for
radiation sensing (Geary and Latham, 1981). The camera is a slow-
scan device which allows frame integration. The detection
characteristics of the device were tested in the 1.5 keV range.
The response was linear with exposure up to ~0.2-0.4 erg/cm^2,
i.e., to far higher intensities than anticipated for auroral
studies.

Primary interest in the CCD for auroral studies is in the
detection of single photons. Resolution of individual photons
with a CCD was originally proposed by Burstein et al. (1978).
Results were first reported by Catura and Smithson (1979) for 5.9
keV and 22.4 keV photons, and by Schwartz et al. (1979) for
energies of 3.0 A keV and above. Resolution of 1.5 keV photons is
more difficult, but it is also of greater relevance to auroral
imaging.

5.2   Experiment

A schematic cross section of a thinned (<10 μm), backside
illuminated silicon CCD is shown in Figure 5-1. Manufactured by
RCA, it is a three-phase, frame transfer device which employs
buried channel technology in both the imaging and transfer-readout
registers. Each pixel has dimensions of 30 μm x 30 μm. The CCD
was cooled to -95°C. A minicomputer controlled operation of the
CCD and processed and displayed the output signals; special
purpose integration and slow-scan readout circuitry, designed for
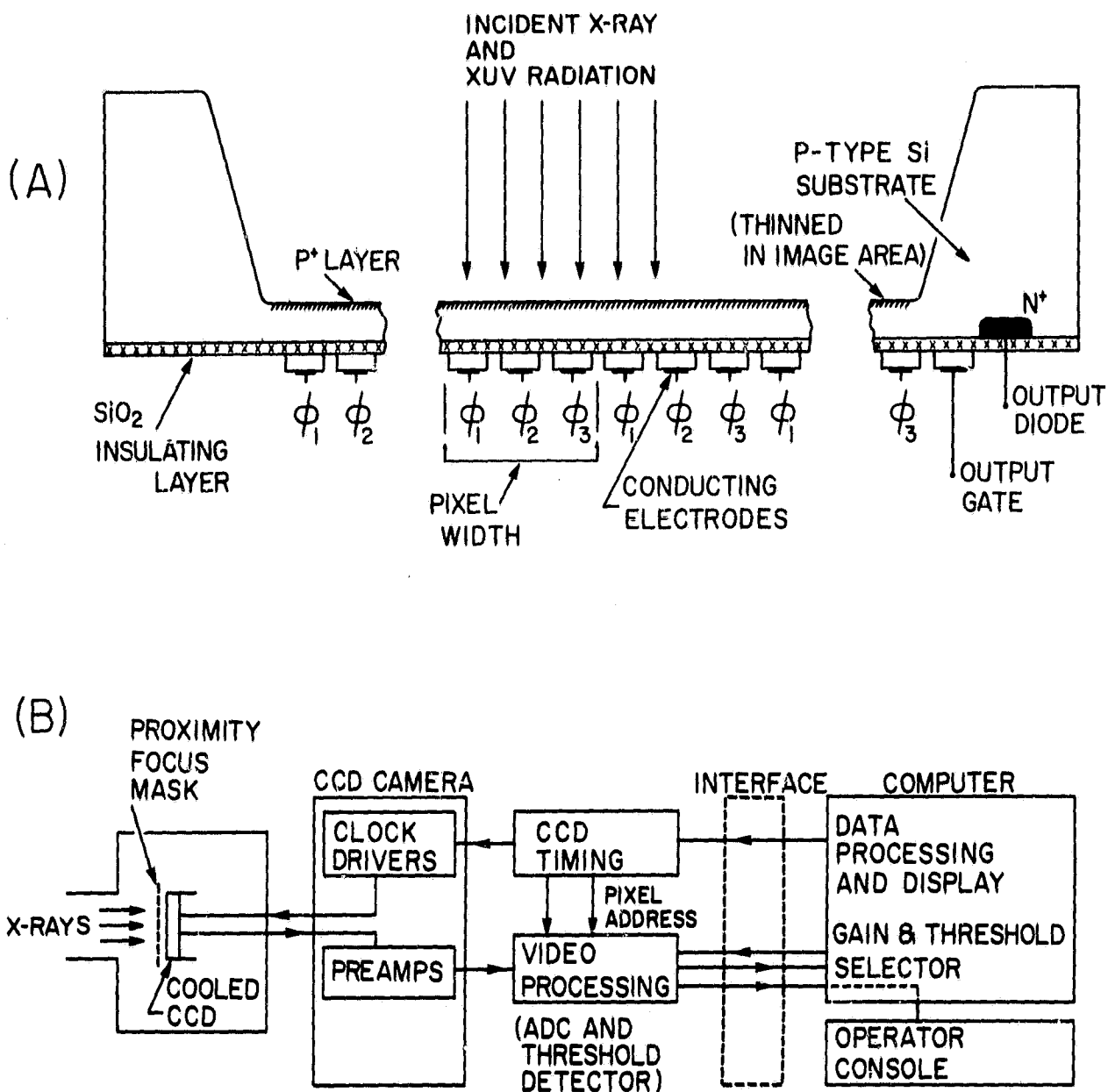flight in a satellite instrument, provided pixel timing signals to
the CCD.

Figure 5-1. Schematic of CCD and control circuitry.

The radiation source was a simple X-ray tube operated with an aluminum anode at 2.0 keV. The source was filtered by an aluminum layer, whose transmission is maximum near the Aℓ Kα line at 1.49 keV. The flux incident on the CCD in photons/cm^2 sec was measured with a gas flow proportional counter to an accuracy of ± 10%. A mask just in front of the CCD was used to form a shadowgraph image of the device; parts of the mask included one to four layers of Kimfol (425 μgm/cm^2 of $C_{16}H_{14}O_3$) to obtain spectral information.

5.3   Results: Exposures > 100 Photons/Pixel

Figure 5-2 shows typical images at exposure levels below and above the saturation threshold for the unfiltered regions of the CCD. The differential filtering produced by the Kimfol can be observed on the right side of the image. The CCD is capable of excellent imaging characteristics, approaching the Nyquist limit of resolution, provided that the capacity of the charge wells is not exceeded.

Figure 5-3 shows averaged response characteristics of the CCD for regions filtered by zero, one, and three layers of Kimfol (respectively marked R_0, R_1, and R_3) with a 64 μm Aℓ filter between source and detector. Response is fully linear with exposure $\bar{N}$ for all three curves for $\bar{N} \lesssim 1200$ photons/pixel. The relative signal levels indicate that there is a considerable bremsstrahlung component in the spectrum in addition to the Aℓ Kα line at 1.49 keV. The attenuation in signal caused by a single Kimfol layer was the same as would be suffered by a mono-energetic 1.24 keV beam.

Assuming an average photon energy of 1.24 keV (which should produce about 350 electron-hole pairs) and a well depth of 240,000 electrons/pixel, we would expect saturation to occur at ~700 photons per pixel if detection efficiency were near unity.

(a) EXPOSURE $\bar{N}$ = 1250 PHOTONS/PIXEL
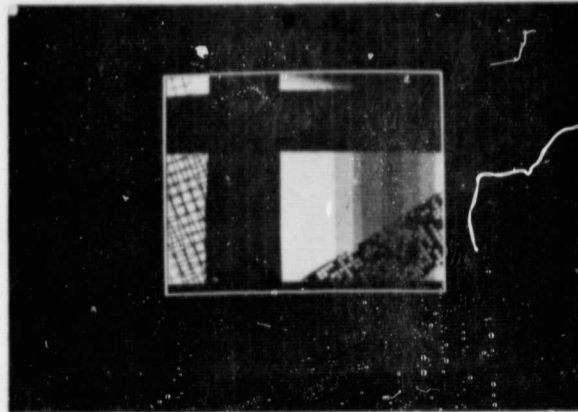
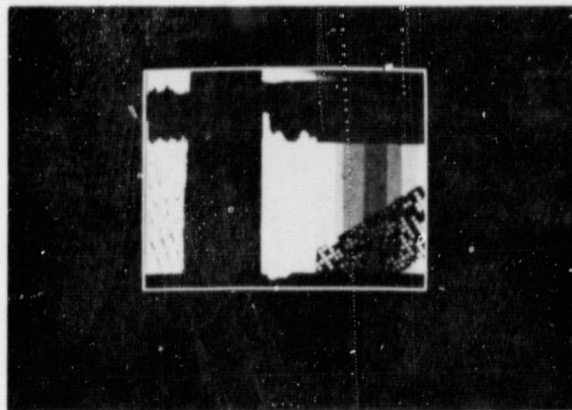## (b) EXPOSURE $\bar{N}$ = 2250 PHOTONS/PIXEL

Figure 5-2. CCD images of mask shadow/attenuation pattern, (a) with no saturation, (b) with the fully exposed regions of the CCD saturated. Period of the screen mesh is 0.33 mm; holes in the lower right quadrant are 0.13 mm squares. Shading on the right side is from differential attenuation by one to four Kimfol layers.

However, the CCD is thin enough that many of these photons passed through it without being absorbed. Our estimated detection efficiency η of 60% is consistent with a depletion layer width of 5 μm, which would absorb 47% of incident 1.49 keV photons and 68% of incident 1.24 keV photons.

Figure 5-3 also characterizes the response amplitude distribution for the unfiltered region of the CCD. If each photon were effectively detected by a single pixel, i.e., with no spreading or leaking from its associated charge packet during the readout process, we would expect a lower limit from photon statistics of $\sigma > (\eta \bar{N})^{-1/2} R_o \approx 1.3 R_o \bar{N}^{-1/2}$; this lower limit is also indicated in Figure 5-3. Additional spreading is expected to arise from the source spectrum and from electron statistics for the bundles of charge generated by the photons. (The background noise of ~ 200 electrons rms for this particular CCD is not significant at these flux levels.) What was actually observed, however, was $\sigma \approx 0.8 R_o \bar{N}^{-1/2}$, considerably below the values predicted by photon statistics. With $(1.3/0.8)^2 \approx 2.6$, we conclude that the charge generated by a given photon was typically read out with significant contributions from three or more pixels; and, typically, no more than half the charge was associated with any given pixel. On the other hand, imaging qualities at the mask edges (Figure 5-2) conclusively show that there is no significant spreading in any direction more than one pixel away from the absorbing pixel. Thus, we conclude that individuals photons were effectively detected by areas of the CCD no larger than 3 x 3 pixels (Loter et al., 1981).

5.4   Attempts to Resolve Single Photons

Attempts were made to directly resolve individual Aℓ Kα photons with a second, quieter CCD chip, which had an rms background noise of less than 100 electrons (vs. 400 electrons expected from a single photon). The thickness of the Aℓ filter between source and

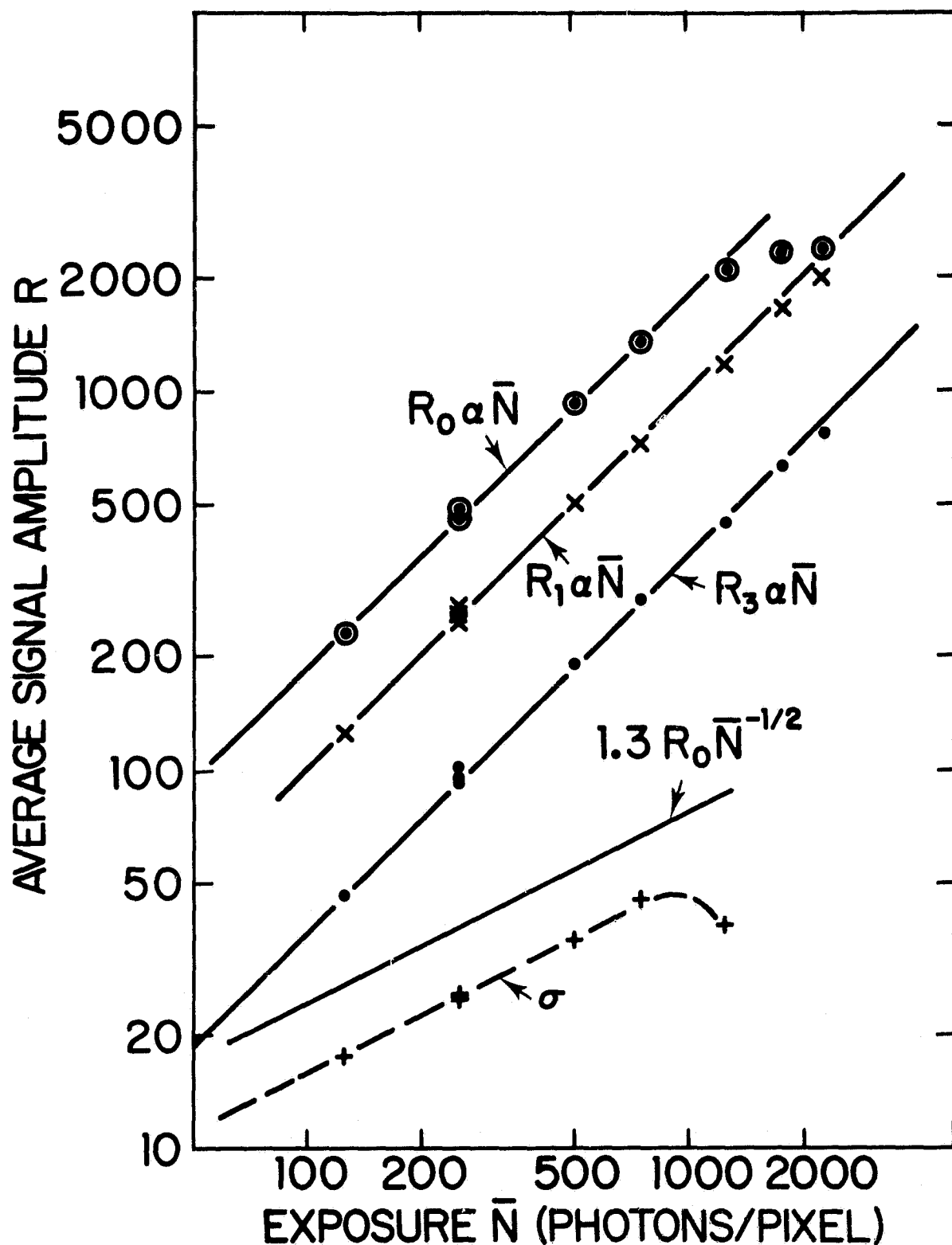Figure 5-3. Top three curves: average signal amplitude R per pixel for differentially filtered regions of the CCD: R_0, no Kimfol; R_1, one 425 μ g/cm^2 layer of Kimfol; R_3, three such Kimfol layers. Bottom two curves: expected minimum spreading of distribution of signal amplitudes, $\sigma = (\eta N)^{-1/2} R_0$, and actual spread parameter σ. One amplitude unit corresponds to 100 ± 10 electrons.

detector was increased to 0.19 mm, increasing the cutoff energy to 1.13 keV (transmission T(1.13 keV) = 0.1 T(1.49 keV)), and the characteristic photon energy to no more than 1.35 keV.

For exposures $N \lesssim 2$ photons pixel, if each photon were effectively resolved by a single pixel, a histogram plot of number of pixels vs. signal amplitude would show mutliple peaks, corresponding to absorption of no photons, one photon, etc., with the widths of the peaks increasing with increasing photon number. Figure 5-4 shows: (a) the actual amplitude distribution for no exposure; (b) the expected shape of the one-photon peak, relative to the zero-photon peak, for exposure $\overline{N}$ = 0.4 photons/pixel, detection efficiency η = 0.55, and effective detection of individual photons by single pixels; and (c) the actual distribution for N = 0.4. It was found that exposures in the range 0.2-2 photons/pixel did not result in a second peak, but rather a shift of the main peak and a progressive lengthening of the tail. As with the other CCD, we conclude that for this CCD no more than half the photon energy is effectively recorded by any one pixel. (Note the lack of pixels at amplitudes greater than +100 in Figure 5-4; we would expect a non-negligible fraction of counts at greater amplitude, from being hit by two or more photons, if more than half the energy were retained, even if the remainder of the energy were spread very widely.)

One possible cause of spreading of charge packets at low exposure levels is trapping of charge at impurity sites or in inhomogene-ities in the potential wells. If such traps release charge on a time scale less than that of the clocking rate, charge packets generated in one pixel can be smeared out over many pixels during readout. However, addition of a light bias corresponding to as much as 2000 electrons/pixel, which might nullify this problem by keeping trapping sites constantly filled, had no apparent effect on the charge spreading phenomena.
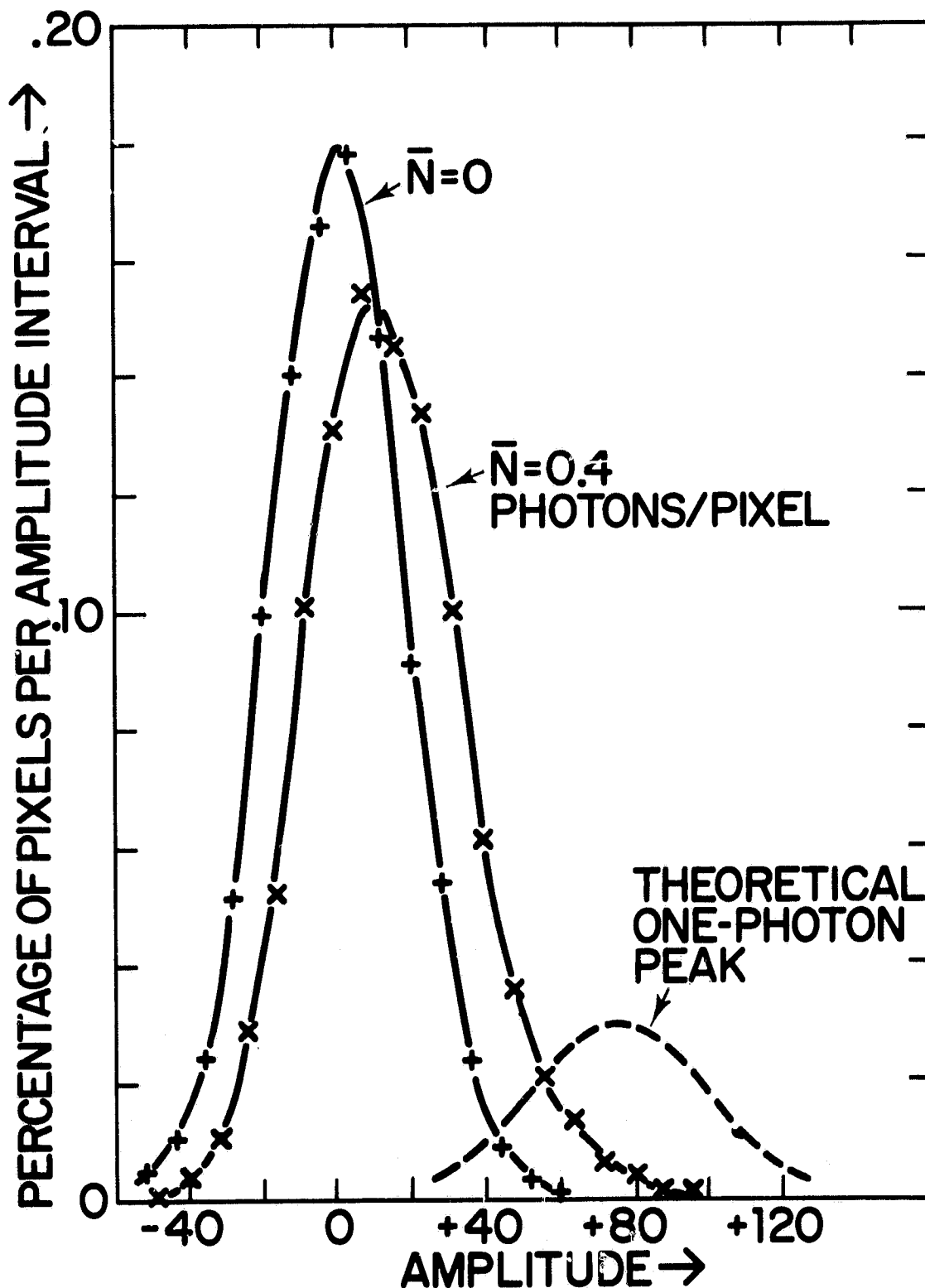
Figure 5-4.   Distribution of pixel response amplitudes (+)
with no exposure; distribution of pixel response
amplitudes (x) for exposure $\bar{N}$ = 0.4 photons/pixel;
theoretical shape of one-photon peak (---) relative
to zero-photon peak for $\bar{N}$ = 0.4 and η = 0.55.   One
amplitude unit corresponds to 5 ± 0.5 electrons.

5-8

Clocking electronics was then altered to read out the data in 3 x
3 "macropixels" by an on-chip summation process: There were three
vertical register clock cycles between each readout of the
horizontal register; during horizontal readout there were three
horizontal register clock cycles for each reset of the charge on
the output transistor gate. No increase in system noise was
observed after the electronics were changed in this manner,
whereas there would effectively be a degradation in the S/N ratio
by a factor of three if the previously-obtained single pixel data
were analyzed in 3 x 3 blocks. Data obtained under these
conditions indicated that the typical spreading of charge
generated by one photon extends over a region of ~ 2 x 2 pixels.

Our results imply that the lower energy limit for effectively
resolving photon energies with RCA CCDs is likely to be several
times greater than would be indicated by rms CCD chip noise. For
example, if it is necessary to analyze single pixel data in 3x3
blocks, signal-to-noise ratio is effectively reduced by a factor
of 3. Depending on where the system noise is generated, this
degradation could be reduced to a factor of 2 by reading out the
data in 2x2 "macropixels" as described above, and then analyzing
those in 2x2 blocks. Such analysis would also require either an
order of magnitude increase in sweeptime, an order of magnitude
reduction in flux, or some combination thereof, to avoid pileup.

We attempted to resolve higher energy photons with two other
CCD's, one manufactured by RCA, the other by Texas Instruments,
Inc. No evidence of single photon resolution could be obtained
with the RCA chip for either titanium K radiation (4.5 keV) or for
5.9 keV X-rays from an Fe -55 source, with and without a light
bias (thought by some to improve charge transfer efficiency), even
for analysis using macropixels; this suggests spreading of charge
packets during transfer considerably beyond a 3 x 3 area. It
should be noted, however, that we operated the TI chips at -140°C.

It is possible that charge transfer efficiency degrades as the CCD is cooled (Zucchino et al., 1981).

The TI CCD chip was a 500 x 500 pixel^2 device with 15μm x 15 μm pixels, thinned to 8-10μm. In one experiment it was exposed to radiation from the X-ray tube, run with a Ti anode at 5.6 kV, and a filter consisting of 38μm Aℓ plus 4.2μm Ti. Therefore, most of the radiation reaching the active CCD surface was in the Ti Kα line at 4.5 keV; the bremsstrahlung energy cutoff of the filter was at 3.6 keV. It can be seen that in the exposed image (Figure 5-5) there are many isolated pixels having amplitudes well above the background level, a characteristic of single photon resolution.

The pixel amplitude distribution (Figure 5-6) shows the expected high amplitude cutoff, corresponding to ~ 1300 electrons. However, the large number of pixels at intermediate values of amplitude is hard to explain, particularly since many represent pixels totally isolated from other pixels above the background level. We conclude that further development on the effects of various clocking or readout parameters in the controlling electronics and their effects on individual chips is required. At a recent conference on the subject of CCD's (Geary and Latham, 1981), some experiments reported successful single photon counting at 5.9 keV, while others reported charge transfer problems, similar to those we encountered. It seems likely that low-level charge transfer characteristics vary from chip to chip, even among chips from the same manufacturer.
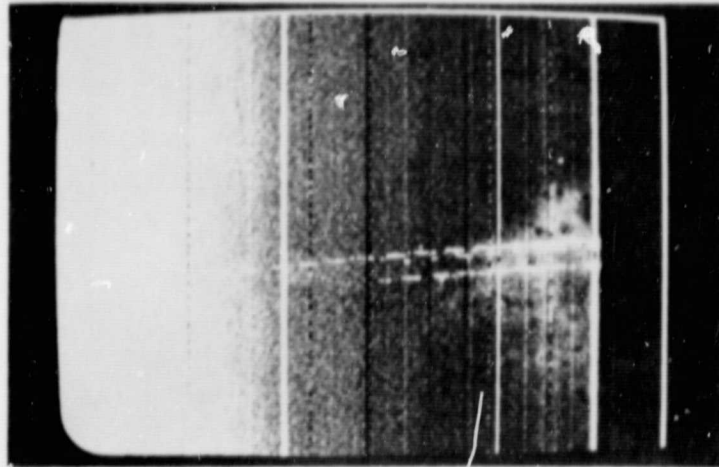
(a.)
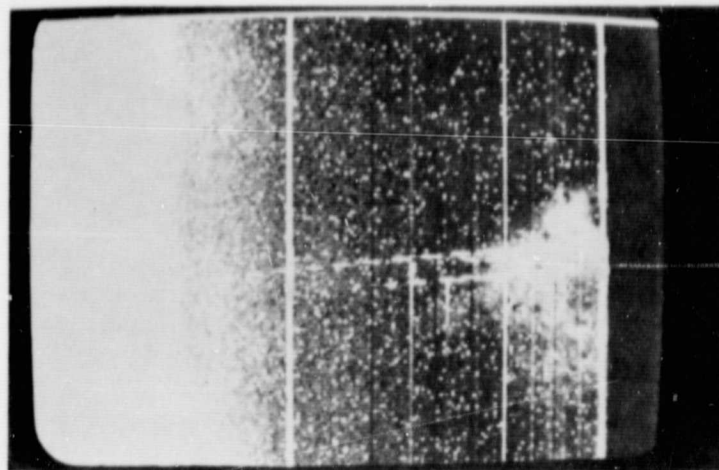
(b.)

Figure 5-5.   Images obtained with the TI CCD showing single photon
impact sites. Top image (a) shows exposure with the
X-ray source off. Bottom image (b) shows sites of
single photons. Large scale variations in the images
are due to flaws in the CCD.
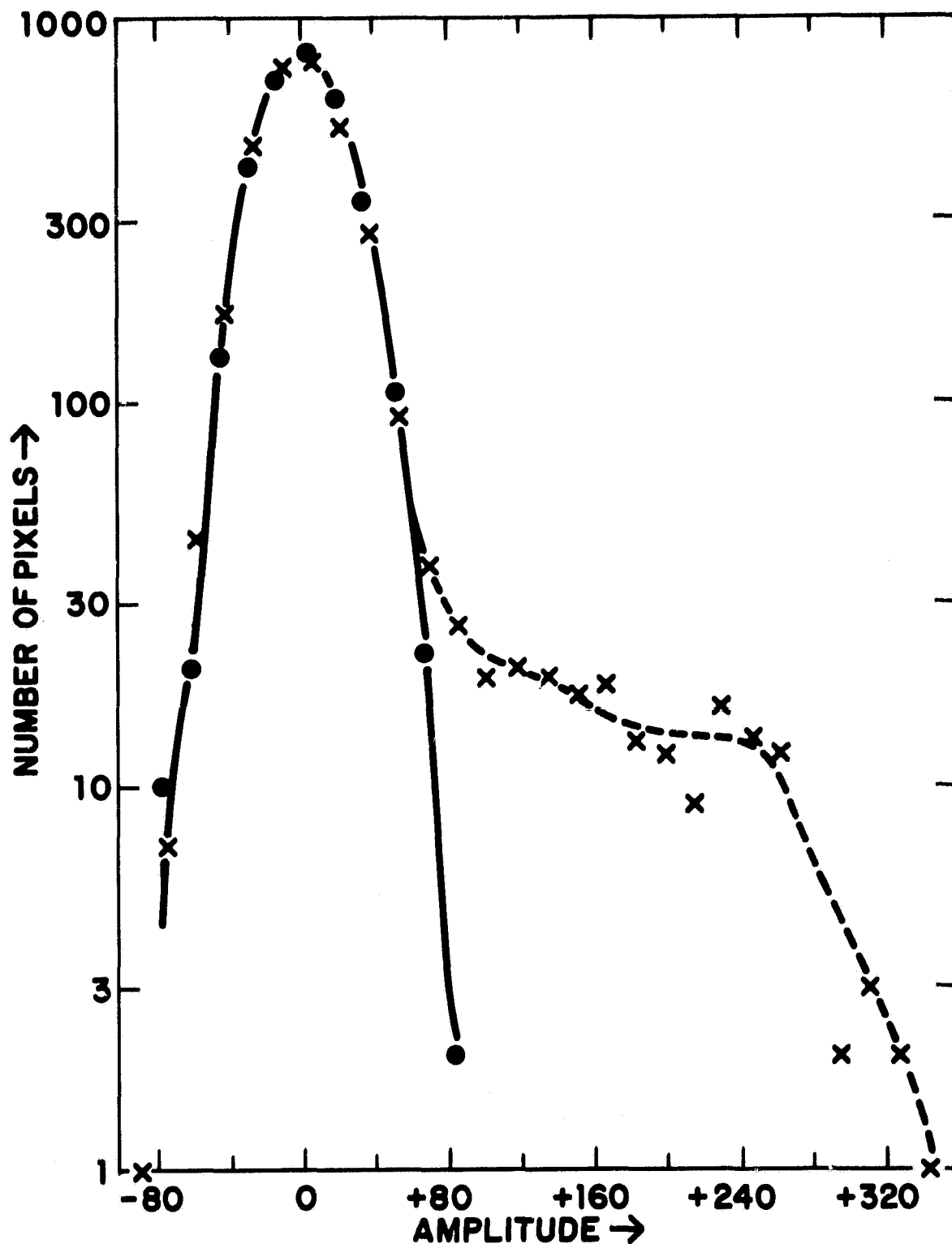
Figure 5-6. Distribution of pixels as a function of signal amplitude from the image shown in Figure 5-5b. One amplitude unit corresponds to 5 ± 0.5 electrons. Solid curve shows pixel response distribution for no exposure. Dashed curve shows distribution resulting from exposure to a 5.9 keV X-ray beam. Note that the signal drops at about 270 amplitude units, corresponding to ~ 5.9 keV.

Despite the inconclusiveness of our experiment, we expect that resolution of single photons near 1 keV will be accomplished in the near future.

Our results with the TI CCD suggest that the charge transfer problems can be corrected in future experiments. The prevailing opinion at RCA is that charge transfer efficiency is degraded at low charge levels primarily by inhomogeneities in potential wells within the pixels; they expect to solve that problem by next year. Operation of recently manufactured RCA CCDs at system noise levels of 15 electrons has been reported (Savoye, 1981); at these noise levels, subkilovolt photons can be resolved with $\Delta E \sim 170$ eV even if charge packets do spread to several pixels.

6.0 EXPERIMENT CONFIGURATION

Figure 6-1 shows the engineering drawing of a practical auroral X-ray telescope (AXT). Table 6-1 summarizes the performance characteristics and the weight, power and telemetry required to achieve the scientific objectives outlined in Section 1.0.

6.1 Optics Fabrication

Following the reasoning in Section 2.0, we concluded that the AXT optics should consist of a coaxial set of seven nested concentric pairs, each with a superpolished nickel-plated beryllium parabolic forward element followed by a hyperboloidal element with the same surface finish. Mirrors can be figured by the single point diamond turning technique. Initial polishing would be done conventionally; the ultimate surface finish of approximately 15 Angstroms RMS can be achieved by a proprietary superpolish process. This method of figuring grazing incidence optics has demonstrated the ability to achieve the 10 arc-second mirror resolution requirement at relatively low cost.

6.2 Subassemblies

6.2.1 Thermal Prefilters

In front of the X-ray mirror aperture is a two-layer thermal pre-filter each layer of which consists of 1000 Angstroms of pure aluminum on a nickel support mesh. The filters serve three major purposes: they prevent contaminants from entering the telescope through the forward apertures, they filter out unwanted white light, and they serve as a thermal barrier to prevent heat loss through the forward apertures.

6.2.2 Visible Aurora Imager

At the center of the X-ray mirror nest is a coaxial dual-element visible aurora imager for obtaining reference optical aurora and
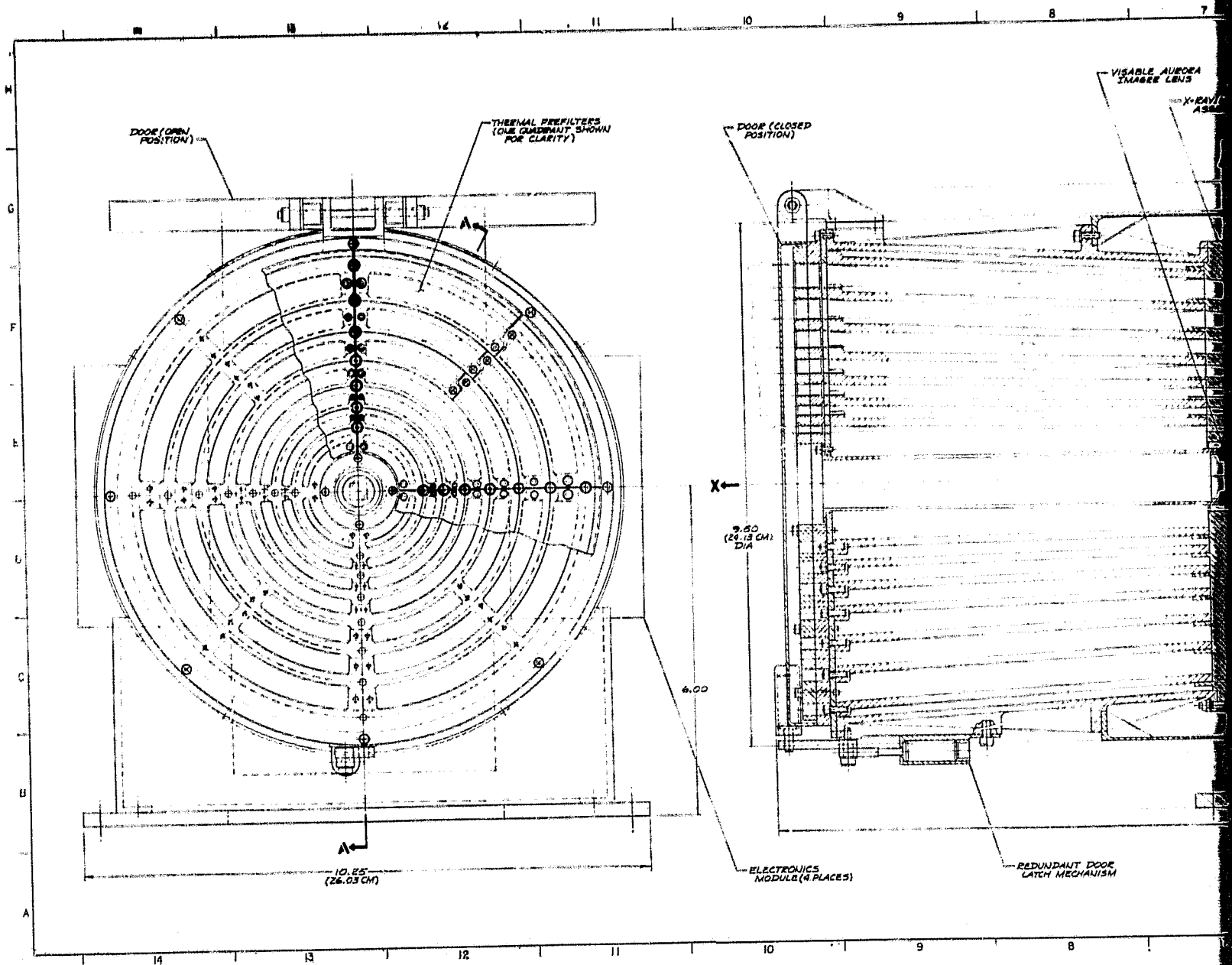
Figure 6-1. Engineering Schematic Layout
Telescope.

6-2

VISABLE AURORA IMAGER LENS

X-RAY MIRROR ASSEMBLY

MIRROR

3.779 FOCAL LENGTH (350 CM)

CCD CAMERA ELECTRONICS

CCD FOCAL PLANE CAMERA

CCD COLDER PLATE

FILTER WHEEL ASSEMBLY

REDUNDANT DOOR LATCH MECHANISM

SECTION A-A

S/C INTERFACE PLANE

24 IN (62.23 CM)

ELECTRONICS

VISIBLE AURORA IMAGER SHUTTER MECHANISM

AURORAL X-RAY TELESCOPE
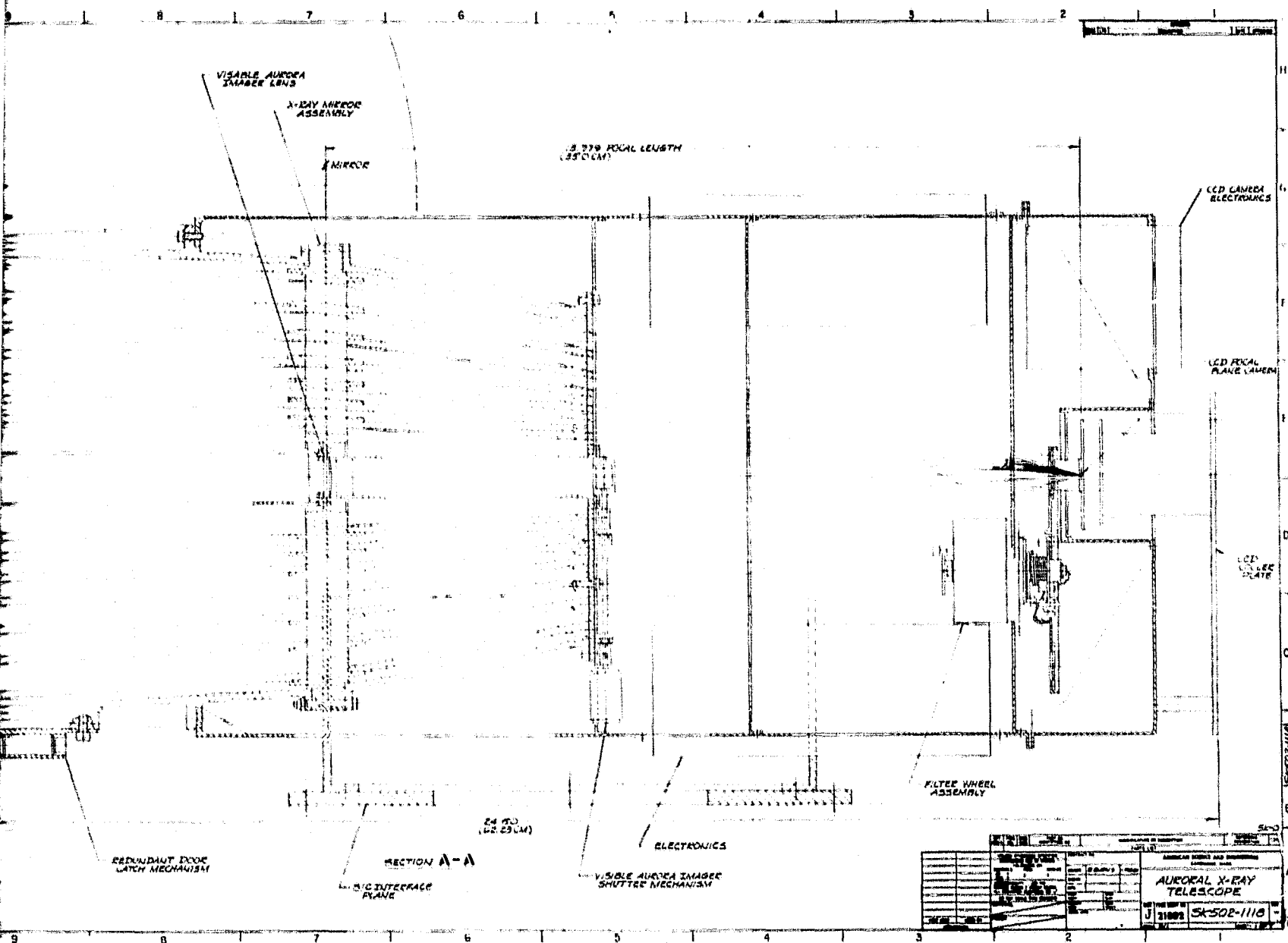
Engineering Schematic Layout of the Auroral X-Ray Telescope.

FOLDOUT FRAME 2

Table 6-1
AURORAL X-RAY TELESCOPE INSTRUMENT SUMMARY

Quantities to be measured	Auroral bremsstrahlung and atomic line emission
X-ray optical system	Wolter Type I grazing incidence telescope
Collecting area	94 cm^2 @ 31.6 Å
Wavelength range	4 - 40 Å (0.3 - 3.0 keV)
Energy resolution	170 eV
Visible-band imager	Doublet lens, coaxial with X-ray optics
Collecting area	2.85 cm^2
Wavelength range	6300 Å (OI) and 4278 Å (N_2^+)
Field of view	1.25 x 1.5 degrees
Detector	Back-illuminated, thinned, charge-coupled device
Detector dark current	< 1 electron/sec/pixel (at −60°C)
Preamp sensitivity	20 photoelectrons rms
Dynamic range	> 10^3
Signal integration time	10 - 1000 sec nominal
Resolution (4 x 4 pixels)	1.2 arc min (30 km at 15 R_E)
Viewing requirements	Up to 15° offset from earth center
Filters	7 band pass filters*
Calibration	Radioactive source on filter wheel
Size	26 x 28 x 63 cm
Weight	20.12 kg
Thermal control	Passive and active (± 5° C)
Memory	700 K bytes
Telemetry/storage rate	5 Kbps average
Power	16.2 watts

---

* Five soft X-ray broadband filters plus 20 Å optical filters at 6303 Å and 4278 Å.

earth limb images. Radiation resistant glass is used for the optical elements. The imager has a mechanical shutter in the optical path to seal out visible light during X-ray exposures. The visible images are otherwise formed on the CCD detector used for X-rays.

6.2.3   CCD Camera

At the focal plane, the image is transformed into an electronic signal by a CCD. The CCD is cooled to reduce the detector dark current. A housing provides structural support for the CCD, radiation shielding, thermal isolation from the warm optical bench, and thermal conduction to a radiative flat-plate cooler on the aft end of the instrument. Mechanically and thermally the CCD system is nearly the same as that developed by AS&E for ISPM (Burstein et al., 1977).

6.2.4   Filter Wheel

Between the X-ray mirror and the CCD there is a ten position filter wheel/shutter. This redundant and failsafe mechanism is virtually identical to that developed by AS&E for the ISPM instrument. Of the ten positions on the wheel, seven are designated for filters, one for a calibration source, one as an open position, and one serves both as a coarse mechanical shutter and as a radiation shield for the CCD. The wheel is driven by a low power (2.3 watts), small angle (4 degree) stepper motor.

6.2.5   Optical Bench

The thin-walled aluminum instrument support structure and optical bench is cylindrical for high structural integrity with minimum weight. To greatly reduce the risk of contaminating the instrument during launch, there is a non-reclosable spring-operated door on the front of the telescope. This lightweight door is opened by a redundant pyrotechnic mechanism similar to that for ISPM. A weight summary for all systems is shown in Table 6-2.

6.2.6 Electronic Packaging and Power Requirements

Electronic packages are mounted around the circumference of the optical bench as shown in Figure 6-1. Video processing electronics for the CCD camera are separately packaged just above the camera itself. The electronic packaging technique is the same as used on ISPM. Table 6-3 shows the estimated electrical power requirements of the various electronic and mechanical systems.

6.2.7 Spacecraft Interface

The spacecraft interface mounting surface is configured to point the telescope optical axis towards the Earth in a direction nominally perpendicular to the spacecraft spin axis. This gives the rear mounted CCD cooler a clear view of deep space for best radiative cooling. Since the experiment is relatively light weight and the pointing requirements are greatly relaxed in comparison to ISPM and other experiments with X-ray telescopes, we anticipate no difficulty in using available three-axis pointing mechanisms.

6.3 Electrical Design and Data Handling

The electrical system consists of the camera system, the microprocessor based control and data handling system, and memory. Memory capacity is sufficient to store ten channels of Pulse Height Analyzer (PHA) data for a 64 x 80 element spectrally dispersed image, one complete 64 x 80 element nondispersed total energy X-ray or visible-light image, and one complete dark current frame. The system also includes motor drivers, interface drivers and receivers, and all required housekeeping signal conditioners and converters. A regulated low voltage power supply derives the necessary operating voltages from the spacecraft power buss. A functional block diagram is shown in Figure 6-2.

Table 6-2
WEIGHT SUMMARY

Component Description	Weight (kg)
X-Ray Mirror Assembly	10.30 kg
CCD Camera nad Cooler	1.32 kg
Mechanisms	0.43 kg
Electronics	4.41 kg
Thermal Control System	0.35 kg
Optical Bench and Door	3.31 kg
	20.12 kg
	(44.36 lbs)

Table 6-3
POWER BUDGET

Component Description	Average Power (Watts)	Peak Power (Watts)
Camera System	1.0	1.0
Pulse Height Analyzer	0.4	0.4
Control and Data Handling	2.5	2.5
Memory and Memory Control	0.5	0.5
Housekeeping	0.2	0.2
Motors and Mechanisms*	0.1	2.4
Interface Circuits	0.2	0.2
Low Voltage Power Supply	3.3	3.3
Subtotal	8.2	10.5
Heater Power	8.0	5.7
TOTAL	16.2	16.2

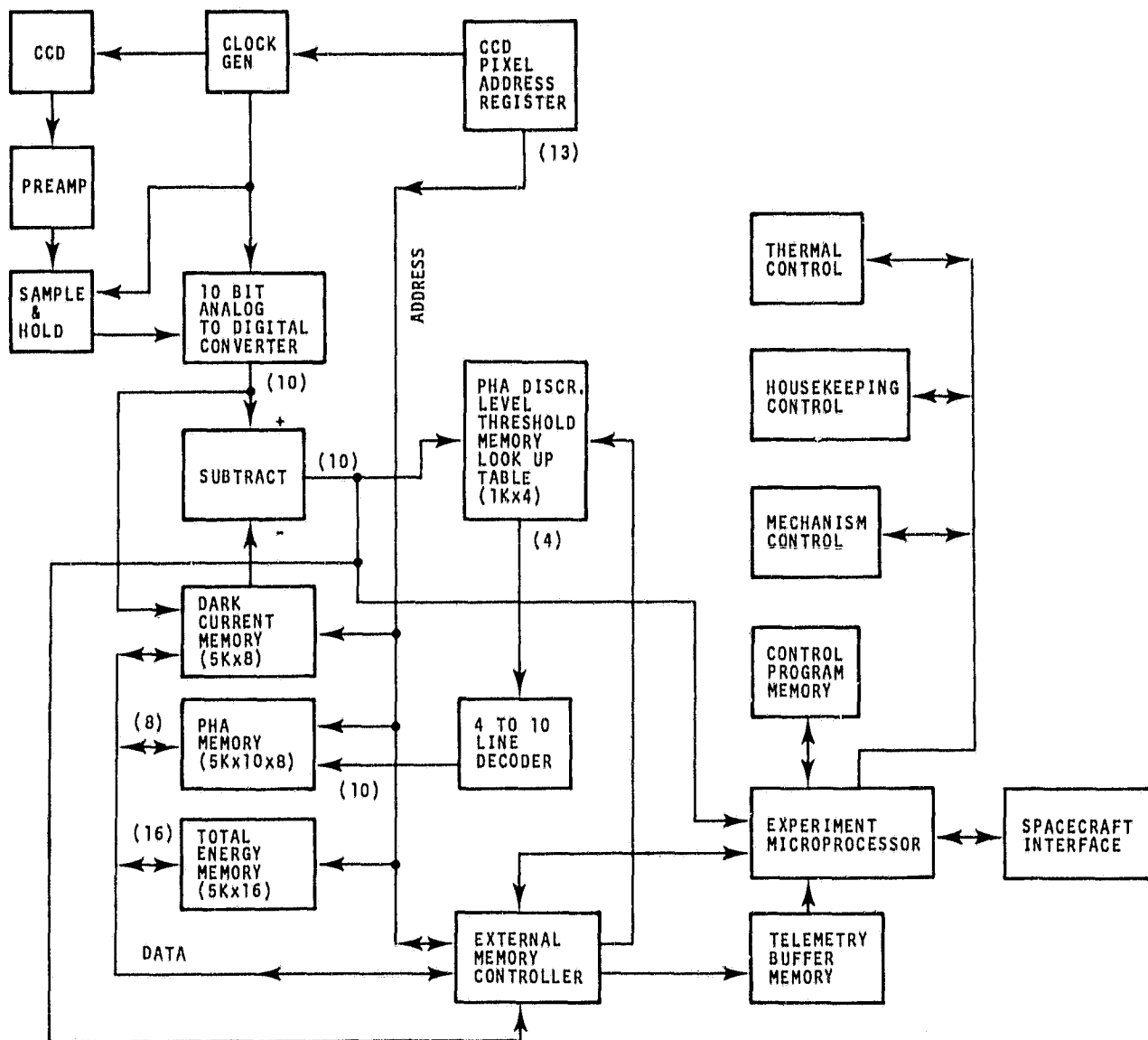*Heater power is temporarily removed while motors draw peak power.

Figure 6-2. Electronics Functional Block Diagram of the
Auroral X-Ray Telescope.

6.3.1   CCD Camera

The heart of the camera system is the buried-channel 256 x 320 picture element ("pixel") RCA CCD at the focus of the telescope. By suitable clocking, the CCD pixels are combined on the chip into "macropixels." In normal operation, the instrument's required spatial resolution is achieved by macropixels consisting of 4 x 4 CCD pixels. Larger macropixels can be obtained on command when desired to reduce telemetry traffic or for other reasons when the resulting loss in spatial resolution is acceptable. A selection of macropixel sizes of 4 x 4, 5 x 5, and 6 x 6 CCD pixels will be easy to provide.

6.3.2   Camera Operation

The CCD integrates photons for an exposure period sufficiently short to make the probability of multiple photon incidences into a macropixel small. The time required to expose and read out a 64 x 80 macropixel frame is approximately 0.25 seconds. At the end of the exposure, the macropixels are sequentially read into a preamplifier. The preamplifier uses a correlated double sampling technique which references each pixel to a stable voltage before readout. The signal-to-noise performance of the circuit is optimized by selecting the duration of the reference level integration and subsequent signal integration. Zero restoration is used to equate the reference level to signal ground voltage, thereby eliminating any out-of-band noise that may be present in the reference voltage. The output signal of the preamplifier thus consists of a pulse for each pixel preceded by a ground reference level. The best signal-to-noise ratio is obtained by integrating and sampling the pulse at a precisely defined time with respect to the last preceding CCD clock pulse transition. The signal is then held and digitized by a 10-bit linear analog-to-digital converter (ADC).

6.3.3 Dark Current Subtraction

The dark current value for each macropixel, stored in a section of digital memory, is subtracted from the ADC reading. The resulting signal is then processed in a ten-channel discriminator and used to increment the appropriate memory addres in the PHA. The dark-current-corrected output signal for each pixel is also linearly added at the appropriate address of the 16-bit "total energy" memory.

6.3.4. PHA Discriminator

The ten-channel discriminator consists of a 1 k x 4 bit memory and a decoder. This memory is loaded with a table corresponding to the 1024 possible ADC output levels. Each level is used to address the memory and access a 4-bit channel number. The channel number is decoded and provides one of 10 memory enable signals which access the memory plane corresponding to the appropriate channel number in the PHA. This memory contains 8 bits for each of the 10 channels of the 5120 pixels. The experiment micro-processor increments the PHA memory channels as well as the total energy memory. Access to all experiment memories outside the microprocessor's normal address space is provided by an external memory controller.

6.3.5 Dark Current Measurement

The signal used to correct the ADC output for dark current is read into memory from the ADC upon ground command while the detector is shielded from incoming radiation. This data also serves as a diagnostic for the health of the CCD and is transmitted to the ground as part of the housekeeping data.

6.3.6 Macropixels

The use of macropixels is an important feature of the proposed design. It reduces to a minimum the proportion of X-ray photons that divide their energy among two or more locations, while still

achieving the required spatial resolution of the instrument. X-ray photons that divide their energy among two or more locations contribute to the apparent low-energy background and add a low energy "tail" to the apparent energy distribution of incident X-rays. The use of macropixels reduces this effect to the point where it ceases to be a concern.

6.3.7   Control and Data Handling System

The microprocessor-based control and data handling system controls the operation of the camera system, the science and housekeeping data acquisition sequences, the storage of data in memory, the transfer of science and housekeeping data to the spacecraft telemetry and data storage system, and the operation of heaters and mechanisms. Program memory is provided partly as "read-only" memory (ROM), partly as random-access memory (RAM). ROM programs are those required by the instrument for initialization and self-protection after power is turned on but before RAM programs have been loaded. RAM programs are configured to simplify the interactions between the instrument and the spacecraft systems while providing the greatest possible flexibility within the instrument. This approach permits altering instrument operating modes in flight to accommodate changing requirements that may be imposed by unexpected results, component degradation, or other considerations.

6.3.8   Memory

Data memory is provided for PHA data (409,600 bits), total energy data (81,920 bits) and for dark current (30,720 bits). In addition, a small amount of memory is provided to support the spacecraft data and command interface and the instrument control function. Like the ISPM instrument, memory for the proposed system is in the form of hybrid CMOS packages with 65,536 bits to a package.

6.4 Thermal Control

The requirements placed upon the thermal control system for this instrument are:

- To maintain the operating temperature of the telescope within a range that retains calibration. For this instrument that range is $20 \pm 50°C$.
- To minimize temperature-gradient induced distortions throughout the instrument and especially within the optical system.
- To cool the CCD and minimize the dark current of the chip. The chip must be cooled to a temperature of $-60°C$ or colder.

6.4.1 Instrument Temperature Control

Overall temperature control is achieved by establishing a balance between external radiation (i.e., sun, earth, spacecraft, etc.), internal heat dissipation (i.e., electronics and designated heaters) and energy emitted or conducted to the surrounding environment. Thermal prefilters are used at the front end of the telescope to control heat losses through the mirror apertures. The entire instrument should be covered with multi-layer insulation (MLI) to minimize uncontrolled radiative heat transfer to the surrounding environment.

6.4.2 Thermal Gradients

The high thermal conductivity of the aluminium optical bench coupled with high emittance black internal surfaces minimize internal gradients throughout the telescope. Conductive thermal isolation from the spacecraft will probably be required to control the effect on the telescope of spacecraft temperature changes. In addition to the electronic power dissipation, heater power of approximately 8.0 watts will be required to thermally control the instrument. This power is allocated to heaters located throughout the instrument by the control and data handling system on the

basis of several temperature monitors. The control program, backed up by a hardware overload protector, will assure that the permissible maximum heater power is never exceeded.

6.4.3   CCD Cooler

To achieve the cold temperature required for proper operation, the CCD is thermally decoupled from the relatively warm (+20°C) optical bench and provided with a radiative cooler of sufficient capacity to overcome residual losses. The thermal design of the camera cooling system is virtually the same as that used for the ISPM instrument which called for a significantly colder temperature (-85°C) than required here (-60°C). Conductive thermal isolation from the optical bench is achieved by a low-conductance support structure. Radiative isolation is obtained through the use of MLI. The radiator plate of the cooler has high thermal emissivity and low solar absorptivity to avoid detector damage if the cooler is accidentally exposed to the sun. A command controlled heater makes it possible to drive off contaminating condensation if this should become necessary during flight.

6.5   Pointing

To achieve the desired scientific objectives it is required that the spacecraft provide a despun platform with relatively precise pointing, knowledge and stability. The knowledge requirement is for 6 arc min accuracy. The stability requirement is for 30 arc-seconds or better over a period of 100 seconds. The expected pointing accuracy of 0.1 degrees is sufficient for the instrument. The mission also requires an off-pointing capability with a range of ± 15 degrees in two orthogonal directions from the nominal axis. Step resolution within this range needs to be 20 arc-minutes.

6.6 Radiation Protection

The radiation environment of the Polar Plasma Laboratory is not precisely known at this time because of its interdependence with the mission orbit. It has been variously estimated between 10^4 and 4×10^6 rads (Si) over the duration of the mission. Depending on where within this range the actual level eventually falls, the radiation problem may be either serious, or almost inconsequential.

Based on our experience designing the White Light Coronagraph and X-Ray/XUV Telescope for the International Solar Polar Mission (which is designed to pass through Jupiter's intense radiation belts), we are confident that radiation will pose no serious difficulty. Shielding against the effects of the Earth's lower energy radiation belts will not be difficult.

Generally we are interested in the effects of radiation on two types of parts: Electronic parts, mainly semiconductors; and optical parts, i.e., glass parts such as lenses. The optical problems are readily resolved through the use of radiation resistant glass. The electronic problems are resolved by a combination of two controls: The use of radiation resistant devices and shielding. For the types of radiation encountered in earth orbit we will be able to shield the electronic boxes and the camera systems to the required levels with a good safety margin without unduly limiting our choice of electronic devices and without seriously impacting the instrument weight. For all critical devices needed for the program we have selected devices used on our International Solar Polar instrument for which shielding guidelines are already available.

7.0   CONCLUSIONS

The basic problems to be confronted in applying X-ray imaging
techniques to study of the aurora are the low flux levels, and the
need to attain good spatial resolution with spectral resolution of
~ 200 eV in the X-ray range near 1 keV. All this must be done
with a lightweight, radiation-hardened instrument that can operate
in earth orbit. On the basis of our studies of the expected
auroral emissions and the noise background, we conclude that a
seven-mirror grazing incidence X-ray telescope of the Wolter
design can collect enough photons to allow spectral imaging of the
aurora over integration periods of 10 to 1000 seconds.

The detector of choice is a thinned, back-illuminated CCD.
Although we were not able to demonstrate unambiguously that single
photon detection (and, therefore, X-ray spectral resolution via
pulse-height distribution analysis) is achievable with the RCA and
TI CCD's available to us, we beleive that the current rapid
development of solid-state detector technology will soon make
single photon counting feasible. There is strong commercial
interest in solid-state detectors and at least three manufacturers
are working on the thinned devices we need for X-ray detection.
The recent conference in Cambridge (Geary and Latham, 1981)
revealed that the manufacturers and various users in the
astronomical community are close to having low noise (6 to 15
electrons per pixel) CCD's in operation.

AS&E is the only organization to attempt photon counting below 1.5
keV. The principal problem plaguing our experiment was charge
transfer inefficiency, that is, some dispersal during readout of
the electrons from the single, pixel-sized packet that should
result from the impact of each X-ray photon. Further experiments
should be conducted, especially with quieter chips operated at
higher temperatures.

Table 6-1 summarizes the capabilities of a practical auroral X-ray
telescope. The spatial resolution requirements for an instrument
on the Polar Plasma Laboratory, at 4-15 Re, for example, are much
reduced from the requirements faced successfully by AS&E in other
programs. Even though the high flux collection requirement led us
to a seven-mirror design, there is no technical obstacle to
construction of a satisfactory telescope.

Experience on the International Solar Polar Program, for which
AS&E is building a CCD-based X-ray telescope, shows that the
necessary electronics and detector can be hardened and/or shielded
adequately against trapped radiation. With adequate precautions,
an auroral telescope experiment should be able to operate for many
years in a terrestrial orbit passing through the radiation belts.

Because auroral X-rays are easily interpreted, X-ray spectral
imaging will be a powerful tool for probing the global
distribution of electron and proton precipitation into the
ionosphere. Further work should be done, however, to study the
transfer of soft X-rays through the upper atmosphere, especially
at the wavelengths of the oxygen and nitrogen K_α lines. Further
discussion of the scientific application of the AXT can be found
in Rust and Burstein (1981) and in the technical section of
American Science and Engineering, Inc. document ASE-4522,
available on request.

APPENDIX I

RMS TECHNIQUE AND RESOLUTION PREDICTION

The Root-Mean-Squared (RMS) averaging technique is an effective
and widely used method of evaluating surface errors in optical
systems. It is used in this report to estimate the blur circle
size of mirror resolution at the focal plane of the mirror systems
described due to environmental effects.

The formula for the RMS value of a set of data is

$$RMS = \left[\sum_{i=1}^{i=n} a_i^2 / n \right]^{1/2}$$

where:

a_i = Value of data point "i";   n = Total number of data points

There are three types of environmental deformation evaluated in
three different manners.

The deformations due to thermal swings evaluated along any
meridian are identical going around the circumference so the RMS
evaluation of the slope errors along any meridian is equivalent to
the RMS slope error of the entire surface. In order to derive the
blur circle size due to this slope error, some operations must be
performed on the RMS slope error. In order to account for the
reflected ray, a factor of 2 must be applied. To account for the
two mirrors in the set, their RMS slope errors are combined in a
square-root-sum of the squares (SRSS) manner.

$$SRSS = \left[\sum_{i=1}^{i=n} a_i^2 \right]^{1/2}$$

a_i = i^{th} item;   n = Number of items

Since the two mirrors in each set are assumed identical, their RMS slope errors are identical. The shift of the incoming ray from the true focus is then:

$$\text{Shift} = \text{RMS Slope} \times 2 \ (= \text{reflection factor})$$
$$\times \sqrt{2} \ (= \text{SRSS summation})$$

This shift is the radius of the blur circle, the resolution is the diameter of the blur circle and can be given as:

$$\text{Resolution} = 2 \times 2 \times \sqrt{2} \ \text{RMS}$$
$$= 5.657 \ \text{RMS}$$

The deformations due to the 1-g ripple along any meridian are not identical going around the circumference. The deformations are maximum at the top and bottom meridians and zero at the sides, dissipating in a cosine function. The RMS slope error for the entire surface is .707 times the RMS slope error evaluated along the worst (top and bottom) meridian. Again taking into account the three factors described for the thermal deformations:

$$\text{Resolution} = 2 \times 2 \times \sqrt{2} \ (.707 \ \text{RMS})$$
$$= 4.0 \ \text{RMS}.$$

The deformation due to the 1-g tilt is a rigid body deformation. The mirrors remain true, but their axes translate and rotate.

A uniform translation of the mirror sets does not affect the resolution. It merely shifts the image on the detector, which can be calibrated. A differential translation between mirror sets effects the resolution in a small way.

$$\text{Resolution} + (\text{Smax} - \text{Smin})/\text{F.L.}$$
$$\text{Smax} = \text{Maximum Translation}$$
$$\text{Smin} = \text{Minimum Translation}$$

The rotation of the mirror in the 1-g tilt is a major contributor to the resolution. Figures A1 and A2 show how the rays are focused at the top and bottom meridians. Figure A1 shows an untilted optic, the parabola surface at an angle α and the hyperbola at an angle β. The incoming rays hit and reflect off the parabola at an angle of α, travelling at an angle to the optical axis of 2α. The rays then hit and reflect off the hyperbola at an angle of $\beta - 2\alpha$, leaving the optic at an angle of $2\beta - 2\alpha$.

Figure A2 shows a mirror system where both optics tilt off the center plate at an angle of Θ. The top meridian of the parabola is now at an angle of $\alpha - \Theta$ and the bottom at $\alpha + \Theta$. The incoming rays hit and reflect off of the parabola at an angle of $\alpha - \Theta$ at the top meridian and travel at $2\alpha - 2\Theta$ to the optical axis, while off the bottom meridian they hit and reflect at $\alpha + \Theta$ and travel at $2\alpha + 2\Theta$. The rays hitting the top meridian hit the hyperbola and reflect off it at an angle of $\beta - 2\alpha + 3\Theta$ and leave the optic at an angle of $2\beta - 2\alpha + 4\Theta$. At the bottom meridian they hit and reflect off the hyperbola at an angle of $\beta - 2\alpha - 3\Theta$ and leave the optic at an angle of $2\beta - 2\alpha - 4\Theta$. The rays from the top and bottom meridians thus focus 4Θ below the undeformed focus.

The sides of the optic are not effected by the tilt as the top and bottom are. The rays hitting the sides of the optic focus at the true focus. Rays-tracing studies carried out on this type deformation show that the image is a ring with no thickness having a diameter of 4Θ and lying tangent to the true focus.
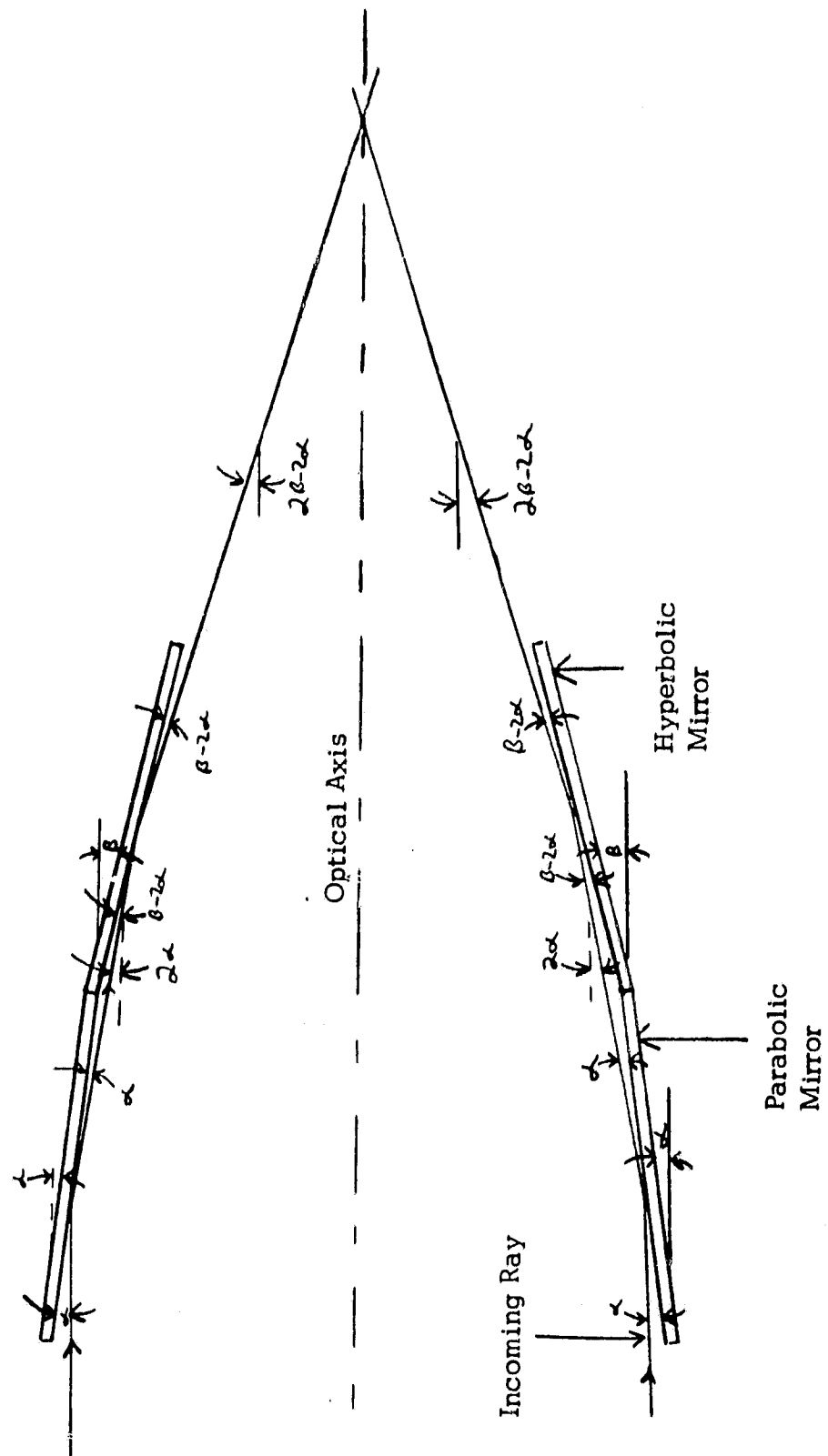
UNDISTORTED MIRRORS

Figure A1.   Undistorted Mirrors.

DISTORTED MIRRORS

Optical Axis

Hyperbolic
Mirror
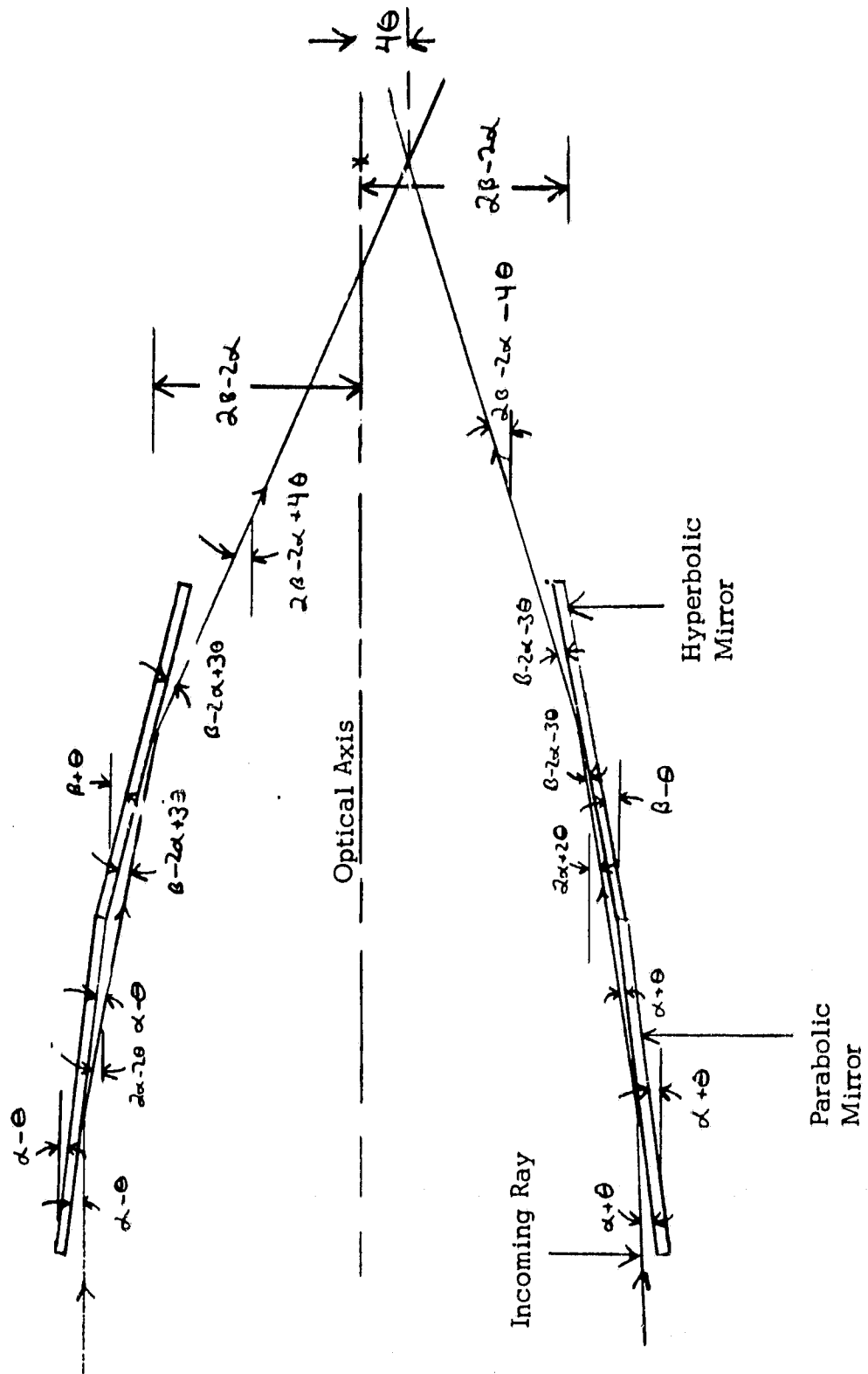
Parabolic
Mirror

Incoming Ray

Figure A-2. Distorted Mirrors.

Since the energy content of this image does not follow a normal distribution the diameter of the blur circle is taken as that which contains 100% of the energy, that is, the effect on resolution of this mode of distortion is 4 Θ where Θ is the tilt angle of the mirrors.

In combining the effect on resolution of the different modes of deformation an SRSS summation is performed.

APPENDIX II

REFERENCES

Burstein, P., R. Hall, B. Holmes, and D. Harrison, The instrument configuration for the white-light coronograph and the X-ray/XUV telescope experiment on the solar polar mission spacecraft, 17th Aerospace Sciences Meeting, A.I.A.A., 1977.

Burstein, P., A. Krieger, M. Vanderhill, and R. Wattson, Soft X-ray imaging experiments with charge-coupled devices (CCDs) and some astronomical applications, Proc. SPIE, 143, 1978.

Catura, R.C. and R.C. Smithson, Single photon X-ray detection with a CCD image sensor, Rev. Sci. Inst., 50, 219, 1979.

Geary, J. and D. Latham (editors), Solid-state Imagers for Astronomy, Proc. SPIE, to be published, 1981.

Loter, N.G., P. Burstein, A. Krieger, D. Ross, and D. Harrison, Soft X-ray and XUV imaging with a CCD-based detector, presented at the SPIE Symposium on Solid-State Imagers for Astronomy, Cambridge, Mass., 1981.

Luhmann, J.G., Auroral bremsstrahlung spectra in the atmosphere, J. Atmos. Terr. Phys., 39, 595, 1977.

Luhmann, J.G. and J.B. Blake, Calculations of soft auroral bremsstrahlung and K_α line emission at satellite altitude, J. Atmos. Terr. Phys., 39, 913,1977.

Luhmann, J.G., H.R. Rugge, J.B. Blake, and L.A. Christopher, Low lattitude atmospheric X-rays observed by HEAO-1, Geophys. Res. Lett., 6, 25, 1979.

Mizera, P.F., J.G. Luhmann, W.A. Kolasinski, and J.B. Blake, Correlated observations of auroral arcs, electrons, and X-rays from a DMSP satellite, J. Geophys. Res., 83, 5573, 1978.

Rugge, H.R., D.L. McKenzie and P.A. Charles, HEAO-1 observations of X-ray fluorescent emission lines from the earth's sunlit atmosphere, Space Research XIX, 243, 1978.

Rust, D.M. and P. Burstein, Application of X-ray imaging techniques to auroral monitoring, Proc. Ionosphere Effects Symp. on Radiowave Systems, Alexandria, VA, 14-16 April 1981.

Savoye, E.D., D.F. Battson, and D.D. Crawshaw, Trends in CCD's for astronomy, SPIE Symp. on Solid State Imagers in Astronomy, Cambridge, Mass., 1981.

Schwartz, D.A., R.E. Griffiths, S.S. Murray, M.V. Zombeck, and W. Bradley, Use of a charge-coupled device in X-ray astronomy as a high resolution imaging detector with spectral resolution, Proc. SPIE, 184, 247, 1979.

Seltzer, S.M. and M.J. Berger, Bremsstrahlung in the atmosphere at satellite altitudes, J. Atmos. Terr. Phys., 36, 1283, 1974.

Van Speybroeck, L.P. and R.C. Chase, Design parameters of paraboloid-hyperboloid telescopes for X-ray astronomy, App. Optics, 11, 440, 1972.

Zucchino, P., D. Long, J.L. Lowrance, G. Renda, D.D. Crawshaw, and D.F. Battson, Evolution of RCA thinned, buried-channel CCD's for scientific applications, SPIE Symp. on Solid State Imagers for Astronomy, Cambridge, Mass., 1981.